A symmetric hybrid formulation for transient wave simulations in PML-truncated heterogeneous media

S. Kucukcoban, L.F. Kallivokas *

Department of Civil, Architectural and Environmental Engineering, The University of Texas at Austin, 1 University Station, C1748, Austin, TX, 78712, USA

ABSTRACT

The numerical simulation of wave motion in arbitrarily heterogeneous semi-infinite media requires the truncation of the semi-infinite extent of the domain to yield a finite computational domain. In the presence of heterogeneity, the domain truncation is best accomplished via the introduction of perfectly-matched-layers (PMLs) at the truncation surface.

By and large, most PML formulations treat in an identical manner both the interior domain and the PML buffer zone. By construction, the complex-coordinate-stretched equations used to introduce the PML, also serve to describe the interior domain, where they reduce to the original, unstretched, system of governing equations. Such a unified treatment, however, results in increased computational cost.

In this development, we discuss a hybrid formulation that leads to a mixed form within the PML, coupled with a standard displacement-only form for the interior domain, both of which are second-order in time. We discuss the formulation and the numerical implementation using finite elements in the context of a standard Galerkin scheme that yields fully symmetric discrete forms, and results in optimal computational cost. We show that existing displacement-based codes for interior domains can be easily modified to accommodate PMLs as a means of domain truncation.

We report on numerical results demonstrating the stability, efficacy, and cost-effectiveness of the hybrid formulation.

1. Introduction

Numerical simulations of wave motion in unbounded domains usually necessitate the reduction of the unbounded domain to a finite computational region via truncation. Truncation, in turn, introduces artificial boundaries that demand special treatment, so that the finite domain of interest ends up mimicking the physics of the originally unbounded domain. Perfectly-matched-layers (PMLs) appear to presently offer the best possible alternative for domain truncation in heterogeneous domains. The PML appears as a buffer zone on the truncation interface, within which outwardly propagating waves are forced to decay with distance into the layer, without reflection from the interior domain-PML interface for all non-zero angles-of-incidence and non-zero frequencies. Spatial discretization introduces numerical reflections, but, in general, the PML's tunable parameters enable the minimization of these reflections. While originally the PML was developed in electromagnetics by splitting fields and recasting second-order PDEs into a system of first-order PDEs [1], the PML's re-interpretation using complex-coordinate-stretching ideas [2] allowed for its rapid development and adoption in other application fields, including acoustics and elastodynamics.

* Corresponding author. Tel.: +1 512 232 5769.
  E-mail addresses: ksezgin@mail.utexas.edu (S. Kucukcoban), loukas@mail.utexas.edu (L.F. Kallivokas).

Table 1
PML implementations in time-domain elastodynamics.

	Split-field	Unsplit-field
FD	Chew and Liu [11], Hastings et al. [12], Liu [13], Collino and Tsogka [14]	Wang and Tang [17], Drossaert and Giannopoulos [22], Komatitsch and Martin [26]
FE/SE	Bécache et al. [15], Komatitsch and Tromp [16], Cohen and Fauqueux [19], Festa and Vilotte [20], Meza-Fajardo and Papageorgiou [24]	Basu and Chopra [18] Kucukcoban and Kallivokas [28]

Naturally, most of the early key developments appeared in electromagnetics: Kuzuoglu and Mitra [3] introduced the, so-called, "complex-frequency-shifted PML" (CFS-PML) by modifying the original form of the stretching function. Using specialized convolutional operations, an efficient implementation of the CFS-PML in electromagnetics was provided in [4], referred to as "convolution PML" (CPML). The generalization of the PML to cartesian, cylindrical, and spherical coordinates was discussed in [5–10]. Chew and Liu in [11] were the first to extend the PML developments from electromagnetics to elastodynamics using a split-field, velocity–stress formulation, implemented using finite differences. Many other implementations of the PML in elastodynamics followed (see e.g., [12–24]). The performance of the PML has been investigated also for Rayleigh and interface waves [25], as well as for near-grazing incident waves [16,22,26,27]. Overall, the literature on PMLs is fairly extensive. Here, our focus is on transient elastodynamics, and to place in context the present development, we summarize in Table 1 the key developments using four classifications: split-field versus unsplit-field formulations, and finite difference versus finite element implementations. In general, when the PML formulation involves split-fields, almost always the resulting scheme is mixed, i.e., both displacements/velocities *and* stresses become unknowns (or some other similar combination, e.g. displacements and strains). One exception is the approach by Komatitsch and Tromp [16], where the displacement field was the only unknown, albeit split into four components. Despite its complexity, their scheme was the first attempt to create a displacement-only PML formulation in elastodynamics. On the other hand, unsplit-field formulations require, in general, the evaluation of convolutions, which, despite the use of recursive or other specialized evaluation schemes, remain expensive. There are two developments that depart from these general trends: first, the work of Basu and Chopra [18] who came close to casting the problem in a non-classic mixed form using unsplit fields, but ended up with a discrete implementation (using finite elements) that destroyed the mixed form, in favor of a complicated time-marching scheme. Their approach seems to retain the displacements as the sole unknown for the interior domain at the expense of the additional storage of strains, and stress and strain time histories per time step. More recently, in [27], Martin et al. have discussed a finite-difference-based method that also retains a displacement-based formulation for the interior domain, and couples it in an *ad hoc* manner with an unsplit staggered velocity–stress formulation of the CPML, the latter similar to the implementation introduced in [20]. The approach in [27] seems to be the most economical proposed to date, in terms of the number of unknowns. Here, using a Galerkin approach, we discuss a coupled weak form for both the interior and PML domains, that leads to a displacement-only form for the interior, and a non-classic mixed form for the PML domain. There results a second-order (in time) fully symmetric discrete system, which can be solved using a standard Newmark time integration scheme. Moreover, the resulting forms allow for the ready incorporation of the PMLs into existing displacement-only finite element codes written for interior domains, despite the mixed form of the PML domain.

We remark that differences in the formulations exist not only with respect to the use of split or unsplit fields, or the underlying numerical method of choice, but also with respect to the choice of the coordinate-stretching function. The latter is a key PML ingredient: from a formulation perspective it affects the temporal complexity, and from a numerical perspective it may affect the simulation accuracy. Specifically, in the case of waves impinging at grazing incidence upon the PML interface, the standard stretching function has been criticized as leading to spurious growths that, over time, may pollute the solution in the interior domain [22,23]. These spurious growths have been shown numerically to exist,[1] and have been loosely attributed to the fact that the stretching function has, by construction, a zero-frequency singularity; however, to date no theoretical proof exists that we are aware of. By contrast, the CPML, which uses the CFS stretching function where the zero-frequency singularity has been removed, has been shown to alleviate the growths, without, however, eliminating them completely [24]. In [24], Meza-Fajardo and Papageorgiou introduced stretching in both coordinate directions within the PML, and showed superior performance of their PML in the case of grazing incidence over both the standard PML and the CPML. Pending more detailed investigations, and since careful PML parameterization has been seen to alleviate the growths, here we too chose to adopt the standard stretching function.

The formulation discussed herein builds and improves upon recently reported work [28]. Specifically, the hybrid formulation we discuss (mixed unsplit-field PML, coupled with a non-mixed approach for the interior domain) leads to

---

[1] The growths can only be seen after the end of the transient phase and only if one were to reduce dramatically the observation scale to several orders of magnitude lower than that of the transient phase. The growths do not appear to be related to a stability issue with the continuous form of the PML, but rather an artifact of its discrete implementation.
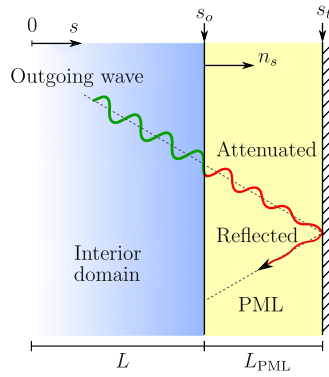
Fig. 1. A PML truncation boundary in the direction of coordinate s.

optimal computational cost over the one presented in [28], and allows for the ready incorporation in existing displacement-based elastodynamics codes.

2. Complex-coordinate-stretching

The original PML formulation [1], was rather restrictive; the interpretation of the PML in the context of complex coordinate-stretching in [2] allowed for the PML's refined development. The idea of complex coordinate-stretching is based on analytic continuation of the solutions of wave equations [10], and is realized via a mapping of the spatial coordinates onto the complex space via complex stretching functions. This is accomplished by a simple change of coordinate variables from real to their *complex-stretched* counterparts. The coordinate change is applied to the equations written in the frequency domain and, if required, the resulting complex-stretched equations are inverted back into the time domain.

We repeat here briefly the key concepts: consider a PML with a layer thickness of L_{PML} attached to the computational domain of interest, as depicted in Fig. 1. Let s denote the coordinate variable defined along the direction normal to the interface located at s_o. The interior domain extends between $0 \leq s < s_o$, and the PML buffer zone occupies $s_o < s \leq s_t$. The key idea is to replace the original coordinate variable s by the *complex-stretched* coordinate $\tilde{s}$ in any equation s appears, where $\tilde{s}$ is defined as

$$\tilde{s} = \int_0^s \varepsilon_s(s', \omega) ds'. \tag{1}$$

In the above, ω denotes circular frequency, and ε_s is a complex stretching function in the direction of coordinate s. The standard PML results when the following form of stretching function is used (which we too adopt herein):

$$\varepsilon_s(s, \omega) = \alpha_s(s) + \frac{\beta_s(s)}{i\omega}, \tag{2}$$

where α_s and β_s denote scaling and attenuation functions, respectively. As the names imply, the real part of ε_s *stretches* or scales s, whereas the imaginary part of ε_s is responsible for the amplitude decay of the propagating wave once it enters the PML. In the case of evanescent waves, α_s stretches the real coordinate, which in turn, becomes responsible for their amplitude decay post PML-entry. Thus, to enforce both propagating and evanescent waves to be attenuated within the PML, we require that $\alpha_s(s) > 1$ and $\beta_s(s) > 0$ be monotonically increasing functions of s. However, in the interior domain we require that $\alpha_s(s) = 1$ and $\beta_s(s) = 0$, so that $\tilde{s} \equiv s$ in the interior domain (no scaling or attenuation within the interior domain). At the interface, continuity between the two domains is satisfied provided $\alpha_s(s_o) = 1$ and $\beta_s(s_o) = 0$. The latter conditions are responsible for ensuring that the interface becomes invisible to the waves entering the PML. Since the scaling and attenuation functions do not depend on frequency, the rate of decay in the PML is frequency-independent. Although α_s is usually taken equal to one, using a value larger than one within the PML improves the attenuation of strong evanescent waves [13].

The form of stretching defined in (2) is not unique and alternative forms were proposed in, for example, [3] (frequency-shifted) and in [29] (second-order). Using either of the latter forms results in a formulation where both the real and imaginary parts of ε_s are now frequency-dependent. Thus, in these cases, the transient implementation of the unsplit-field PML would involve convolutory terms. As discussed in the introduction, in this work the standard stretching function is preferred. Moreover, (2) leads to a straightforward implementation and exhibits better performance than the CPML with low-frequency propagating waves that are commonly encountered in seismology and geotechnical investigations.

Lastly, with the aid of the fundamental theorem of calculus, there also holds that

$$\frac{d\tilde{s}}{ds} = \frac{d}{ds} \int_0^s \varepsilon_s(s', \omega) ds' = \varepsilon_s(s, \omega) \Rightarrow \frac{d}{d\tilde{s}} = \frac{1}{\varepsilon_s(s, \omega)} \frac{d}{ds}. \tag{3}$$

Relation (3) will be used to transform the governing equations.

There is no rigorous methodology suggested in the literature for choosing α_s and β_s, but to minimize reflections, generally, quadratic or higher profiles should be used. It is also common practice to use similar profiles for both scaling and attenuation functions. The form of the scaling and attenuation profiles, in terms of a polynomial of arbitrary degree m, is

$$\alpha_s(s) = \begin{cases} 1, & 0 \leq s \leq s_o, \\ 1 + \alpha_o \left[\dfrac{(s - s_o)n_s}{L_{\text{PML}}} \right]^m, & s_o < s < s_t, \end{cases} \tag{4a}$$

$$\beta_s(s) = \begin{cases} 0, & 0 \leq s \leq s_o, \\ \beta_o \left[\dfrac{(s - s_o)n_s}{L_{\text{PML}}} \right]^m, & s_o < s < s_t, \end{cases} \tag{4b}$$

where α_o and β_o are user-chosen scalar parameters, m is the degree of the polynomial attenuation, and n_s is the s-th component of the outward normal to the interface between the PML and the interior domain. For ε_s to remain dimensionless, parameter α_o must be dimensionless, whereas parameter β_o must have units of frequency. The optimal values of these parameters are critical for the PML performance [30,31]. However, such an explicit form for optimal (α_o, β_o) remains elusive due to its strict dependence on both the data and the discretization of the problem at hand. There are very few reported attempts in the literature, where the PML parameters are sought to be optimized, and none that we are aware of for time-domain elastodynamics. For example, in [30] Collino and Monk discussed a numerical optimization approach for determining optimal PML parameters for all angles of incidence and various PML lengths in the context of frequency-domain electromagnetics. In [31], Bermúdez et al. proposed, in the context of frequency-domain acoustics, a singular attenuation function for the PML that exhibits a power-type singularity at the PML termination boundary, which seems to eliminate the PML's performance dependence on discretization parameters. In [14], Collino and Tsogka proposed the following form for β_o, based on one-dimensional wave propagation ideas,

$$\beta_o = \frac{(m + 1)V_R}{2L_{\text{PML}}} \log \left(\frac{1}{R} \right), \tag{5}$$

where R is user-tunable reflection coefficient controlling the amount of reflections from the outer PML boundary, that is typically set as fixed, and V_R is, in general, a reference velocity. Though (5) is not the optimal choice, it associates the problem data, to some extent, with the imposed attenuation profile. Here, we use β_o to control the attenuation intensity.

We note that, once discretized, the PML is not reflectionless anymore and requires an optimal choice for $\alpha_s(s)$ and $\beta_s(s)$ such that the shape of the imposed attenuation profile within the PML could be adequately resolved by the discretization in order to minimize spurious reflections. In general, the polynomial order m in (4) controls the shape of the attenuation profile within the PML: depending on the order, a sharper transition could be imposed either closer to the PML-interior domain interface, or closer to the fixed PML boundary. This, in turn, drives the meshing within the PML. Moreover, the scalar factor β_o in front of the polynomial term controls the intensity of the imposed attenuation. However, it cannot be chosen arbitrarily large; in fact, the larger β_o is, the larger the discretization errors become, such that the solution in the interior domain may become polluted.

To quantify our observations, we turn our attention to the amplitude decay factor (ADF) for the propagating waves:

$$(\text{ADF}) = e^{-\frac{k}{\omega} \int_0^s \beta(s') ds'} = e^{-\beta_o n_s^m \left(\frac{L_{\text{PML}}}{m+1} \right) \left(\frac{s - s_o}{L_{\text{PML}}} \right)^{m+1}}. \tag{6}$$

Fig. 2(a) shows the amplitude decay of the propagating waves within a normalized PML length for a fixed polynomial order ($m = 2$): with increasing β_o, the decay profile becomes sharper close to the regular domain-PML interface. By contrast, Fig. 2(b) shows that the profile becomes sharper closer to the outer fixed PML boundary with increasing polynomial order m.

Therefore, the upper limits for β_o and m depend on the mesh. In this work, for the numerical results, we use β_o to control the attenuation intensity within the PML for a fixed polynomial order $m = 2$. We also provide results for various β_0 values. For notational brevity, the functional dependence of ε_s, α_s and β_s will be henceforth omitted.

3. Two-dimensional unsplit-field PML

The propagation of linear elastic waves is governed by the equations of motion, the generalized Hooke's law, and the kinematic conditions:

$$\textbf{div } \mathcal{S}^T + \mathbf{f} = \rho \ddot{\mathbf{u}}, \tag{7a}$$

$$\mathcal{S} = \mathcal{C}[\mathcal{E}], \tag{7b}$$

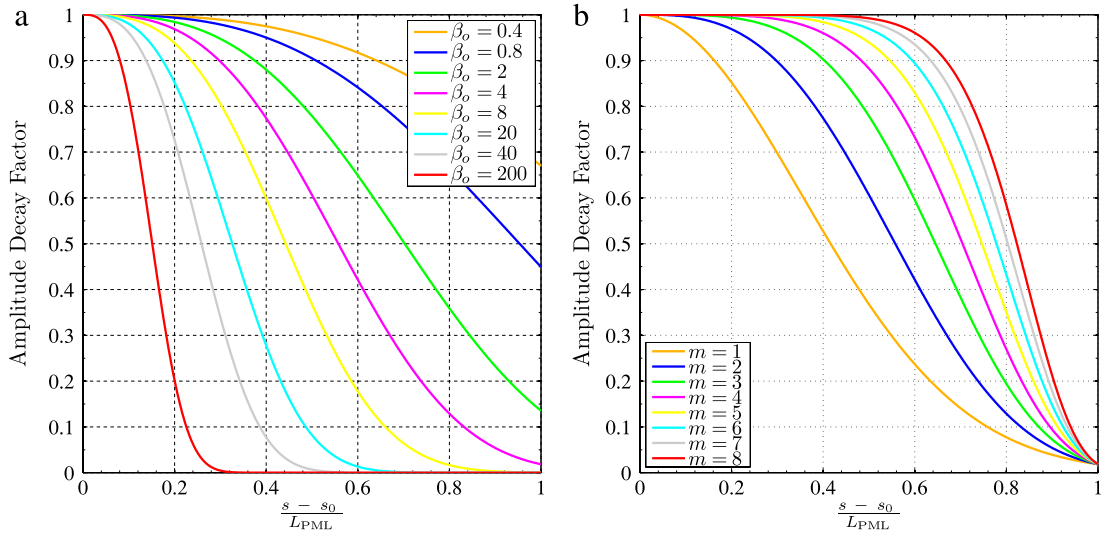$$\mathcal{E} = \frac{1}{2} \left[\nabla \mathbf{u} + (\nabla \mathbf{u})^T \right], \tag{7c}$$

Fig. 2. Attenuation of the propagating waves within the PML for (a) various β_o, fixed polynomial order $m = 2$, (b) fixed $\beta_o = 4$, various polynomial orders m.

where $\mathcal{S}$, $\mathcal{E}$, and $\mathcal{C}$ are the stress, strain, and elasticity tensors, respectively[2]; ρ is the density of the elastic medium, **u** is the displacement vector, **f** is the load vector, (:) denotes tensor inner product, and a dot (˙) denotes differentiation with respect to time of the subtended function.

The PML formulation originates from the application of complex coordinate-stretching to the governing equations. The stretched equations govern the motion within both the interior and PML domains, on the grounds that, within the interior domain, they reduce, by construction of the stretching function ε_s, to the original (unstretched) system of governing equations. To obtain the PML formulation, Eqs. (7a)–(7c) must first be Fourier-transformed, then stretched, and finally inverted back into the time-domain for transient implementations. In what follows, we shall initially make no distinction between the interior domain and the PML buffer, and use the complex-stretched equations for both domains. The distinction, which, in effect, allows for the hybrid treatment, will be made at a later stage.

3.1. Frequency-domain equations

First, the equilibrium, constitutive, and kinematic equations (7a)–(7c) are Fourier-transformed into the frequency-domain, to obtain

$$\textbf{div}\ \hat{\mathcal{S}}^T + \hat{\mathbf{f}} = -\omega^2 \rho \hat{\mathbf{u}}, \tag{8a}$$

$$\hat{\mathcal{S}} = \mathcal{C}[\hat{\mathcal{E}}], \tag{8b}$$

$$\hat{\mathcal{E}} = \frac{1}{2}\left[\nabla \hat{\mathbf{u}} + \left(\nabla \hat{\mathbf{u}}\right)^T\right], \tag{8c}$$

where a caret (ˆ) denotes the Fourier transform of the subtended function, and the spatial and frequency dependence of the vector and tensor quantities are implicit. In deriving (8a), we assumed initially silent conditions for the displacement field. Next, we complex-stretch each coordinate per:

$$\tilde{x} = \int_0^x \varepsilon_x(x')dx', \quad \varepsilon_x = \alpha_x + \frac{\beta_x}{i\omega}, \qquad \frac{d}{d\tilde{x}} = \frac{1}{\varepsilon_x}\frac{d}{dx}, \tag{9a}$$

$$\tilde{y} = \int_0^y \varepsilon_y(y')dy', \quad \varepsilon_y = \alpha_y + \frac{\beta_y}{i\omega}, \qquad \frac{d}{d\tilde{y}} = \frac{1}{\varepsilon_y}\frac{d}{dy}. \tag{9b}$$

The stretching is applied first to the equations of motion (8a) by replacing x and y with the stretched coordinates $\tilde{x}$ and $\tilde{y}$; to clarify, we make use of unabridged notation:

---

[2] Throughout, the square brackets following a fourth-order tensor such as $\mathcal{C}$ imply tensor operation of a fourth-order on the second-order tensor within the square brackets. For the isotropic case, $\mathcal{C}[\mathcal{E}] = 2\mu\mathcal{E} + \lambda(\text{tr}\mathcal{E})\mathcal{I}$, where λ and μ are the Lamé parameters, and $\mathcal{I}$ is the identity tensor.

$$\frac{\partial \hat{\mathscr{s}}_{xx}}{\partial \tilde{x}} + \frac{\partial \hat{\mathscr{s}}_{yx}}{\partial \tilde{y}} + \hat{f}_x = -\omega^2 \rho \hat{u}_x, \tag{10a}$$

$$\frac{\partial \hat{\mathscr{s}}_{xy}}{\partial \tilde{x}} + \frac{\partial \hat{\mathscr{s}}_{yy}}{\partial \tilde{y}} + \hat{f}_y = -\omega^2 \rho \hat{u}_y, \tag{10b}$$

where $\mathscr{s}_{ij}$ denotes stress tensor component. Making use of (9), (10) can be written in terms of the physical (non-stretched) coordinates as

$$\frac{1}{\varepsilon_x} \frac{\partial \hat{\mathscr{s}}_{xx}}{\partial x} + \frac{1}{\varepsilon_y} \frac{\partial \hat{\mathscr{s}}_{yx}}{\partial y} + \hat{f}_x = -\omega^2 \rho \hat{u}_x, \tag{11a}$$

$$\frac{1}{\varepsilon_x} \frac{\partial \hat{\mathscr{s}}_{xy}}{\partial x} + \frac{1}{\varepsilon_y} \frac{\partial \hat{\mathscr{s}}_{yy}}{\partial y} + \hat{f}_y = -\omega^2 \rho \hat{u}_y. \tag{11b}$$

Next, we multiply both sides of (11) by $\varepsilon_x \varepsilon_y$; there results

$$\mathbf{div} \left(\hat{\mathscr{s}}^T \tilde{\Lambda} \right) + \varepsilon_x \varepsilon_y \hat{\mathbf{f}} = -\omega^2 \rho \varepsilon_x \varepsilon_y \hat{\mathbf{u}}, \tag{12}$$

in which the tensor $\tilde{\Lambda}$ is defined as (the definition is identical to that used in [18])

$$\tilde{\Lambda} = \begin{bmatrix} \varepsilon_y & 0 \\ 0 & \varepsilon_x \end{bmatrix} = \begin{bmatrix} \alpha_y & 0 \\ 0 & \alpha_x \end{bmatrix} + \frac{1}{i\omega} \begin{bmatrix} \beta_y & 0 \\ 0 & \beta_x \end{bmatrix} = \tilde{\Lambda}_e + \frac{1}{i\omega} \tilde{\Lambda}_p, \tag{13}$$

and the subscripts "e" and "p" refer to attenuation functions associated with evanescent and propagating waves, respectively. Within the interior domain, $\tilde{\Lambda}_e$ reduces to the identity tensor, whereas $\tilde{\Lambda}_p$ vanishes identically. After substituting (13) and (9) into (12), rearranging and grouping like-terms, there results

$$\mathbf{div} \left(\hat{\mathscr{s}}^T \tilde{\Lambda}_e + \frac{1}{i\omega} \hat{\mathscr{s}}^T \tilde{\Lambda}_p \right) + \left[a\hat{\mathbf{f}} + \frac{b}{i\omega} \hat{\mathbf{f}} + \frac{c}{(i\omega)^2} \hat{\mathbf{f}} \right] = \rho \left[(i\omega)^2 a\hat{\mathbf{u}} + i\omega b\hat{\mathbf{u}} + c\hat{\mathbf{u}} \right], \tag{14}$$

where

$$a = \alpha_x \alpha_y, \qquad b = \alpha_x \beta_y + \alpha_y \beta_x, \qquad c = \beta_x \beta_y. \tag{15}$$

We note that, within the interior domain, $a \equiv 1, b \equiv 0, c \equiv 0$, and since the body forces $\mathbf{f}$ are non-zero only within the interior domain, (14) reduces further to

$$\mathbf{div} \left(\hat{\mathscr{s}}^T \tilde{\Lambda}_e + \frac{1}{i\omega} \hat{\mathscr{s}}^T \tilde{\Lambda}_p \right) + a\hat{\mathbf{f}} = \rho \left[(i\omega)^2 a\hat{\mathbf{u}} + i\omega b\hat{\mathbf{u}} + c\hat{\mathbf{u}} \right]. \tag{16}$$

Similarly, we apply complex coordinate-stretching to the kinematic equation (8c); there results

$$\hat{\varepsilon} = \frac{1}{2} \left\{ (\nabla \hat{\mathbf{u}}) \begin{bmatrix} \dfrac{1}{\varepsilon_x} & 0 \\ 0 & \dfrac{1}{\varepsilon_y} \end{bmatrix} + \begin{bmatrix} \dfrac{1}{\varepsilon_x} & 0 \\ 0 & \dfrac{1}{\varepsilon_y} \end{bmatrix} (\nabla \hat{\mathbf{u}})^T \right\}. \tag{17}$$

Next, we multiply (17) by $i\omega \varepsilon_x \varepsilon_y$ to obtain

$$i\omega \varepsilon_x \varepsilon_y \hat{\varepsilon} = \frac{1}{2} i\omega \left[(\nabla \hat{\mathbf{u}}) \tilde{\Lambda} + \tilde{\Lambda} (\nabla \hat{\mathbf{u}})^T \right], \tag{18}$$

where the (complex) stretching tensor $\tilde{\Lambda}$ is defined in (13). Substituting (13) and (9) into (18), rearranging and grouping like-terms, results in

$$i\omega a\hat{\varepsilon} + b\hat{\varepsilon} + \frac{1}{i\omega} c\hat{\varepsilon} = \frac{1}{2} \left[(\nabla \hat{\mathbf{u}}) \tilde{\Lambda}_p + \tilde{\Lambda}_p (\nabla \hat{\mathbf{u}})^T \right] + \frac{1}{2} i\omega \left[(\nabla \hat{\mathbf{u}}) \tilde{\Lambda}_e + \tilde{\Lambda}_e (\nabla \hat{\mathbf{u}})^T \right]. \tag{19}$$

Eqs. (16), (8b) and (19), constitute the stretched form of the governing frequency-domain equations.

We note that the operation in (18) is not unique; for example, one could pre- and post-multiply (17) by $i\omega \Lambda^{-T}$ and Λ^{-1}, respectively, similarly to what was done in [18], to obtain

$$i\omega \Lambda^{-T} \hat{\varepsilon} \Lambda^{-1} = \frac{1}{2} i\omega \left[\Lambda^{-T} (\nabla \hat{\mathbf{u}}) + (\nabla \hat{\mathbf{u}})^T \Lambda^{-1} \right], \tag{20}$$

where

$$\Lambda^{-1} = \begin{bmatrix} \varepsilon_x & 0 \\ 0 & \varepsilon_y \end{bmatrix} = \begin{bmatrix} \alpha_x & 0 \\ 0 & \alpha_y \end{bmatrix} + \frac{1}{i\omega} \begin{bmatrix} \beta_x & 0 \\ 0 & \beta_y \end{bmatrix} = \Lambda_e + \frac{1}{i\omega} \Lambda_p. \tag{21}$$

Using the latter definition results in

$$i\omega \Lambda_e^T \hat{\mathcal{E}} \Lambda_e + \Lambda_e^T \hat{\mathcal{E}} \Lambda_p + \Lambda_p^T \hat{\mathcal{E}} \Lambda_e + \frac{1}{i\omega} \Lambda_p^T \hat{\mathcal{E}} \Lambda_p = \frac{1}{2} \left[\Lambda_p^T (\nabla \hat{\mathbf{u}}) + (\nabla \hat{\mathbf{u}})^T \Lambda_p \right] + \frac{1}{2} i\omega \left[\Lambda_e^T (\nabla \hat{\mathbf{u}}) + (\nabla \hat{\mathbf{u}})^T \Lambda_e \right], \quad (22)$$

which differs considerably from (19). The use of (19) instead of (22) as the stretched kinematic condition, entails advantages, the most important of which is that we retain the same coefficients on both the left-side of (19) and the right-side of (16). Specifically, the similar stretching of equilibrium and kinematic equations (both multiplied by $\varepsilon_x \varepsilon_y$), manifests itself in the symmetry of the resulting forms. Thus, upon discretization, the semi-discrete forms become fully-symmetric in contrast to the non-symmetric form predicated upon (22) and used in [18,28].

3.2. Time-domain equations

Next, we are interested in inverting the stretched frequency-domain equations back into the time-domain. To aid in the development, we make use of the following Fourier transform valid for any function $g(t)$ satisfying the usual requirements:

$$\mathcal{F}^{-1} \left[\frac{\hat{g}(\omega)}{i\omega} \right] = \int_0^t g(\tau) d\tau, \quad (23)$$

where $\mathcal{F}^{-1}$ denotes the inverse Fourier operator.[3] With the aid of (23), the inverse Fourier transforms of (16), (8b) and (19), written for both the interior and PML domains, become

$$\mathbf{div} \left[\mathcal{S}^T \tilde{\Lambda}_e + \left(\int_0^t \mathcal{S}^T d\tau \right) \tilde{\Lambda}_p \right] + a\mathbf{f} = \rho \left(a\ddot{\mathbf{u}} + b\dot{\mathbf{u}} + c\mathbf{u} \right), \quad (24a)$$

$$\mathcal{S} = \mathcal{C}[\mathcal{E}], \quad (24b)$$

$$a\dot{\mathcal{E}} + b\mathcal{E} + c \left(\int_0^t \mathcal{E} d\tau \right) = \frac{1}{2} \left[(\nabla \mathbf{u}) \tilde{\Lambda}_p + \tilde{\Lambda}_p (\nabla \mathbf{u})^T + (\nabla \dot{\mathbf{u}}) \tilde{\Lambda}_e + \tilde{\Lambda}_e (\nabla \dot{\mathbf{u}})^T \right]. \quad (24c)$$

Now, we introduce auxiliary variables $\mathbf{S}(\mathbf{x}, t)$ and $\mathbf{E}(\mathbf{x}, t)$, similar to what we had done in earlier work [28,32], which physically represent stress and strain memories or histories, defined as

$$\mathbf{S}(\mathbf{x}, t) = \int_0^t \mathcal{S}(\mathbf{x}, \tau) d\tau, \qquad \mathbf{E}(\mathbf{x}, t) = \int_0^t \mathcal{E}(\mathbf{x}, \tau) d\tau. \quad (25a)$$

Clearly,

$$\dot{\mathbf{S}}(\mathbf{x}, t) = \mathcal{S}(\mathbf{x}, t), \qquad \ddot{\mathbf{S}}(\mathbf{x}, t) = \dot{\mathcal{S}}(\mathbf{x}, t), \quad (25b)$$

$$\dot{\mathbf{E}}(\mathbf{x}, t) = \mathcal{E}(\mathbf{x}, t), \qquad \ddot{\mathbf{E}}(\mathbf{x}, t) = \dot{\mathcal{E}}(\mathbf{x}, t). \quad (25c)$$

Thus, substituting (25) into (24) and combining the constitutive equation with the kinematic equation yields the time-domain equations:

$$\mathbf{div} \left(\dot{\mathbf{S}}^T \tilde{\Lambda}_e + \mathbf{S}^T \tilde{\Lambda}_p \right) + a\mathbf{f} = \rho \left(a\ddot{\mathbf{u}} + b\dot{\mathbf{u}} + c\mathbf{u} \right), \quad (26a)$$

$$\mathcal{D} \left[\left(a\ddot{\mathbf{S}} + b\dot{\mathbf{S}} + c\mathbf{S} \right) \right] = \frac{1}{2} \left[(\nabla \mathbf{u}) \tilde{\Lambda}_p + \tilde{\Lambda}_p (\nabla \mathbf{u})^T + (\nabla \dot{\mathbf{u}}) \tilde{\Lambda}_e + \tilde{\Lambda}_e (\nabla \dot{\mathbf{u}})^T \right], \quad (26b)$$

where $\mathcal{D}$ denotes the compliance tensor ($\mathcal{E} = \mathcal{D}[\mathcal{S}]$).

4. Hybrid formulation

Eqs. (26) could only be reduced to a single (vector) equation implicating a single field (displacements) at the expense of the temporal complexity, which would, in that case, involve convolutory terms. To maintain the second-order character of (26), a mixed method is adopted, whereby both displacements and stresses (or, more appropriately, stress histories) are retained as unknowns. Subsequently, a unified treatment of both the interior and PML domains would have been a natural choice, and indeed this has been the choice in many PML formulations. Then, however, the mixed method becomes fairly expensive and is redundant for the interior (regular) domain. Here, we propose a hybrid approach,[4] whereby we retain a displacement-only interior problem, and couple it with the mixed formulation for the unsplit-field PML. Thus, the wave motion in the PML-truncated domain (Fig. 3) is governed by the following system of equations:

---

[3] In general, $\mathcal{F}^{-1} \left[\frac{\hat{g}(\omega)}{i\omega} \right] = \int_0^t g(\tau) d\tau - \pi \hat{g}(0)\delta(\omega)$, but, it can be shown that since, by construction, the overall development excludes $\omega = 0$, the inverse transform reduces to (23).

[4] We use *hybrid* to imply the coupling of a non-mixed with a mixed formulation.
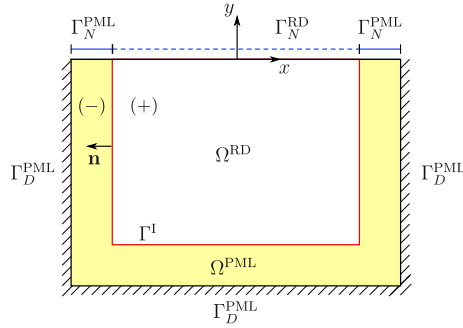
Fig. 3. PML-truncated semi-infinite domain.

$$\textbf{div}\,\left\{\mu\left[\nabla\mathbf{u}+(\nabla\mathbf{u})^T\right]+\lambda(\text{div}\,\mathbf{u})\mathcal{I}\right\}+\mathbf{f}=\rho\ddot{\mathbf{u}}\quad\text{in }\Omega^{\text{RD}}\times\mathsf{J},\tag{27a}$$

$$\textbf{div}\,\left(\dot{\mathbf{S}}^T\tilde{\varLambda}_e+\mathbf{S}^T\tilde{\varLambda}_p\right)=\rho\,(a\ddot{\mathbf{u}}+b\dot{\mathbf{u}}+c\mathbf{u})\quad\text{in }\Omega^{\text{PML}}\times\mathsf{J},\tag{27b}$$

$$\mathcal{D}\left[\left(a\ddot{\mathbf{S}}+b\dot{\mathbf{S}}+c\mathbf{S}\right)\right]=\frac{1}{2}\left[(\nabla\dot{\mathbf{u}})\tilde{\varLambda}_e+\tilde{\varLambda}_e(\nabla\dot{\mathbf{u}})^T+(\nabla\mathbf{u})\tilde{\varLambda}_p+\tilde{\varLambda}_p(\nabla\mathbf{u})^T\right]\quad\text{in }\Omega^{\text{PML}}\times\mathsf{J},\tag{27c}$$

subject to silent initial conditions, and the following boundary and interface conditions:

$$\left\{\mu\left[\nabla\mathbf{u}+(\nabla\mathbf{u})^T\right]+\lambda(\text{div}\,\mathbf{u})\mathcal{I}\right\}\mathbf{n}=\mathbf{g}_n\quad\text{on }\varGamma_N^{\text{RD}}\times\mathsf{J},\tag{28a}$$

$$(\dot{\mathbf{S}}^T\tilde{\varLambda}_e+\mathbf{S}^T\tilde{\varLambda}_p)\mathbf{n}=\mathbf{0}\quad\text{on }\varGamma_N^{\text{PML}}\times\mathsf{J},\tag{28b}$$

$$\mathbf{u}=\mathbf{0}\quad\text{on }\varGamma_D^{\text{PML}}\times\mathsf{J},\tag{28c}$$

$$\mathbf{u}^+=\mathbf{u}^-\quad\text{on }\varGamma^I\times\mathsf{J},\tag{28d}$$

$$\left\{\mu\left[\nabla\mathbf{u}+(\nabla\mathbf{u})^T\right]+\lambda(\text{div}\,\mathbf{u})\mathcal{I}\right\}\mathbf{n}=-(\dot{\mathbf{S}}^T\tilde{\varLambda}_e+\mathbf{S}^T\tilde{\varLambda}_p)\mathbf{n}\quad\text{on }\varGamma^I\times\mathsf{J},\tag{28e}$$

where time/space dependences are implicit, and $\Omega\subset\mathbb{R}^2$ denotes the region occupied by the elastic body (Ω^{RD}),[5] surrounded on three of its sides by the PML buffer zone (Ω^{PML}). $\varGamma^I$ is the interface boundary between the regular and PML domains. Ω is bounded by $\varGamma=\varGamma_D\cup\varGamma_N$, where $\varGamma_D\cap\varGamma_N=\emptyset$, and $\varGamma_D\equiv\varGamma_D^{\text{PML}}$, $\varGamma_N=\varGamma_N^{\text{RD}}\cup\varGamma_N^{\text{PML}}$. Moreover, $\mathbf{g}_n$ denotes prescribed tractions and $\mathsf{J}=(0,T)$ denotes the time interval of interest. Note that body forces $\mathbf{f}$ in (26a) vanish inside the PML domain and, therefore, disappear from (27b).

We seek next the weak form, in the Galerkin sense, corresponding to the strong form (27)–(28). There are two possible weak forms one could derive for the mixed problem at hand (see discussion in [28]). The only difference between the two possible formulations arises from the judicious application of integration by parts, which results in *decidedly different* regularity requirements for the approximants [33]. A classic mixed form arises when one seeks a weak form by integrating by parts the combined constitutive and kinematic equation (27c), while not integrating by parts the equilibrium equation (27b). In this first form the regularity required for the stress approximants is higher than that of the displacement approximants; this is the classic mixed method requiring the use of specialized elements (RT, BDM, MINI, PEERS, etc.). On the other hand, in the second form, which differs from the first simply by an integration by parts applied instead only to the equilibrium equation (27b), while retaining without integration by parts (27c), the regularity requirements are somewhat reversed. The latter requirements are less onerous for implementation purposes and do not require any specialized element types. Similarly to [28], here too we use this second weak form. Specifically, we take inner products of (27) with test functions $\mathbf{w}_1(\mathbf{x})$, $\mathbf{w}_2(\mathbf{x})$ and $\mathbf{T}(\mathbf{x})$, and then integrate over Ω^{RD}, Ω^{PML} and Ω^{PML}, respectively, where the integration by parts is applied to the equilibrium equations (27a) and (27b). By adding the equilibrium equations, the weak form of (27) can be cast as

$$\int_{\Omega^{\text{RD}}}\nabla\mathbf{w}_1:\left\{\mu\left[\nabla\mathbf{u}+(\nabla\mathbf{u})^T\right]+\lambda(\text{div}\,\mathbf{u})\mathcal{I}\right\}\,d\Omega+\int_{\Omega^{\text{PML}}}\nabla\mathbf{w}_2:\left(\dot{\mathbf{S}}^T\tilde{\varLambda}_e+\mathbf{S}^T\tilde{\varLambda}_p\right)d\Omega$$

$$+\int_{\Omega^{\text{RD}}}\mathbf{w}_1\cdot\rho\ddot{\mathbf{u}}\,d\Omega+\int_{\Omega^{\text{PML}}}\mathbf{w}_2\cdot\rho\,(a\ddot{\mathbf{u}}+b\dot{\mathbf{u}}+c\mathbf{u})\,d\Omega=\int_{\varGamma_N^{\text{RD}}}\mathbf{w}_1\cdot\mathbf{g}_n\,d\varGamma+\int_{\Omega^{\text{RD}}}\mathbf{w}_1\cdot\mathbf{f}\,d\Omega,\tag{29a}$$

$$\int_{\Omega^{\text{PML}}}\mathbf{T}:\left[\mathcal{D}\left[\left(a\ddot{\mathbf{S}}+b\dot{\mathbf{S}}+c\mathbf{S}\right)\right]\right]d\Omega=\frac{1}{2}\int_{\Omega^{\text{PML}}}\mathbf{T}:\left[(\nabla\dot{\mathbf{u}})\tilde{\varLambda}_e+\tilde{\varLambda}_e(\nabla\dot{\mathbf{u}})^T+(\nabla\mathbf{u})\tilde{\varLambda}_p+\tilde{\varLambda}_p(\nabla\mathbf{u})^T\right]d\Omega.\tag{29b}$$

---

[5] RD stands for Regular (interior) Domain.

We seek $\mathbf{u} \in \mathbf{H}^1(\Omega) \times \mathsf{J}$ satisfying $\mathbf{u}|_{\Gamma_D^{\mathrm{PML}}} = \mathbf{0}$, and $\mathbf{S} \in \mathscr{L}^2(\Omega) \times \mathsf{J}$, such that Eq. (29) holds for all $\mathbf{w}_1 \in \mathbf{H}^1(\Omega)$, $\mathbf{w}_2 \in \mathbf{H}^1(\Omega)$ satisfying $\mathbf{w}|_{\Gamma_D^{\mathrm{PML}}} = \mathbf{0}$ and $\mathbf{T} \in \mathscr{L}^2(\Omega)$. The functional spaces of relevance here are defined, as usual, for scalar- (v), vector- ($\mathbf{v}$), and tensor-valued ($\mathcal{A}$) functions, via

$$L^2(\Omega) = \left\{ v \colon \int_{\Omega} |v|^2 d\mathbf{x} < \infty \right\}, \tag{30a}$$

$$\mathscr{L}^2(\Omega) = \left\{ \mathcal{A} \colon \mathcal{A} \in (L^2(\Omega))^{2 \times 2} \right\}, \tag{30b}$$

$$H^1(\Omega) = \left\{ v \colon \int_{\Omega} \left(|v|^2 + |\nabla v|^2 \right) d\mathbf{x} < \infty \right\}, \tag{30c}$$

$$\mathbf{H}^1(\Omega) = \left\{ \mathbf{v} \colon \mathbf{v} \in (H^1(\Omega))^2 \right\}. \tag{30d}$$

It is important to notice that the regularity required for the stresses is *lower* than that of the displacements. In the numerical experiments, we used linear–linear, quadratic–linear, and quadratic–quadratic pairs without observing stability difficulties.

For the mixed finite element implementation of the weak form (29), both $\mathbf{u}(\mathbf{x}, t)$ and $\mathbf{S}(\mathbf{x}, t)$ are treated as independent variables that need to be approximated separately. Let the basis functions residing in $\mathbf{\Xi}_h \subset \mathbf{H}^1(\Omega)$ and $\mathbf{\Upsilon}_h \subset \mathscr{L}^2(\Omega)$ be denoted by $\mathbf{\Phi}$ and $\mathbf{\Psi}$, respectively. The trial functions $\mathbf{u}_h \in \mathbf{\Xi}_h \times \mathsf{J}$, and $\mathbf{S}_h \in \mathbf{\Upsilon}_h \times \mathsf{J}$ are spatially discretized as

$$\mathbf{u}(\mathbf{x}, t) \cong \mathbf{u}_h(\mathbf{x}, t) = \begin{bmatrix} \mathbf{\Phi}^T(\mathbf{x})\mathbf{u}_x(t) \\ \mathbf{\Phi}^T(\mathbf{x})\mathbf{u}_y(t) \end{bmatrix}, \tag{31a}$$

$$\mathbf{S}(\mathbf{x}, t) \cong \mathbf{S}_h(\mathbf{x}, t) = \begin{bmatrix} \mathbf{\Psi}^T(\mathbf{x})\mathbf{S}_{xx}(t) & \mathbf{\Psi}^T(\mathbf{x})\mathbf{S}_{xy}(t) \\ \mathbf{\Psi}^T(\mathbf{x})\mathbf{S}_{yx}(t) & \mathbf{\Psi}^T(\mathbf{x})\mathbf{S}_{yy}(t) \end{bmatrix}. \tag{31b}$$

Similarly, the test functions $\mathbf{w}_1, \mathbf{w}_2 \in \mathbf{\Xi}_h$ and $\mathbf{T} \in \mathbf{\Upsilon}_h$ are expressed as

$$\mathbf{w}_1(\mathbf{x}) \cong \mathbf{w}_{1h}(\mathbf{x}) = \begin{bmatrix} \mathbf{w}_{1x}^T \mathbf{\Phi}(\mathbf{x}) \\ \mathbf{w}_{1y}^T \mathbf{\Phi}(\mathbf{x}) \end{bmatrix}, \tag{32a}$$

$$\mathbf{w}_2(\mathbf{x}) \cong \mathbf{w}_{2h}(\mathbf{x}) = \begin{bmatrix} \mathbf{w}_{2x}^T \mathbf{\Phi}(\mathbf{x}) \\ \mathbf{w}_{2y}^T \mathbf{\Phi}(\mathbf{x}) \end{bmatrix}, \tag{32b}$$

$$\mathbf{T}(\mathbf{x}) \cong \mathbf{T}_h(\mathbf{x}) = \begin{bmatrix} \mathbf{T}_{xx}^T \mathbf{\Psi}(\mathbf{x}) & \mathbf{T}_{xy}^T \mathbf{\Psi}(\mathbf{x}) \\ \mathbf{T}_{yx}^T \mathbf{\Psi}(\mathbf{x}) & \mathbf{T}_{yy}^T \mathbf{\Psi}(\mathbf{x}) \end{bmatrix}. \tag{32c}$$

To reduce notational congestion, we henceforth drop the time and space dependences. We, subsequently, obtain the following *semi-discrete form*

$$\mathbf{M}\ddot{\mathbf{d}} + \mathbf{C}\dot{\mathbf{d}} + \mathbf{K}\mathbf{d} = \mathbf{F}, \tag{33}$$

where the system matrices $\mathbf{M}$, $\mathbf{C}$, $\mathbf{K}$, and the system vectors $\mathbf{d}$ and $\mathbf{F}$ are defined as

$$\mathbf{M} = \begin{bmatrix} \mathbf{M}^{rr} & \mathbf{M}^{ri} & \mathbf{0} & \mathbf{0} & \mathbf{0} \\ & \mathbf{M}_a^{ii} & \mathbf{M}_a^{ip} & \mathbf{0} & \mathbf{0} \\ & & \mathbf{M}_a^{pp} & \mathbf{0} & \mathbf{0} \\ & sym & & \mathbf{N}_a^{ii} & \mathbf{N}_a^{ip} \\ & & & & \mathbf{N}_a^{pp} \end{bmatrix}, \qquad \mathbf{C} = \begin{bmatrix} \mathbf{0} & \mathbf{0} & \mathbf{0} & \mathbf{0} & \mathbf{0} \\ & \mathbf{M}_b^{ii} & \mathbf{M}_b^{ip} & \mathbf{A}^{ii} & \mathbf{A}^{ip} \\ & & \mathbf{M}_b^{pp} & \mathbf{A}^{pi} & \mathbf{A}^{pp} \\ & sym & & \mathbf{N}_b^{ii} & \mathbf{N}_b^{ip} \\ & & & & \mathbf{N}_b^{pp} \end{bmatrix}, \tag{34a}$$

$$\mathbf{K} = \begin{bmatrix} \mathbf{Q}^{rr} & \mathbf{Q}^{ri} & \mathbf{0} & \mathbf{0} & \mathbf{0} \\ & \mathbf{M}_c^{ii} & \mathbf{M}_c^{ip} & \mathbf{B}^{ii} & \mathbf{B}^{ip} \\ & & \mathbf{M}_c^{pp} & \mathbf{B}^{pi} & \mathbf{B}^{pp} \\ & sym & & \mathbf{N}_c^{ii} & \mathbf{N}_c^{ip} \\ & & & & \mathbf{N}_c^{pp} \end{bmatrix}, \tag{34b}$$

$$\mathbf{d} = \begin{bmatrix} \mathbf{u}^r & \mathbf{u}^i & \mathbf{u}^p & \mathbf{S}^i & \mathbf{S}^p \end{bmatrix}^T, \qquad \mathbf{F} = \begin{bmatrix} \mathbf{f}^r & \mathbf{f}^i & \mathbf{0} & \mathbf{0} & \mathbf{0} \end{bmatrix}^T, \tag{34c}$$

with r, i, and p representing *regular* (interior) domain, *interface*, and *PML* domain, respectively. The various submatrices in the above expression are constructible by using standard Lagrange polynomial approximations (see the Appendix, Eqs. (A.1)–(A.3)), and account for the imposed wave amplitude attenuation within the PML domain. Note that the upper-left
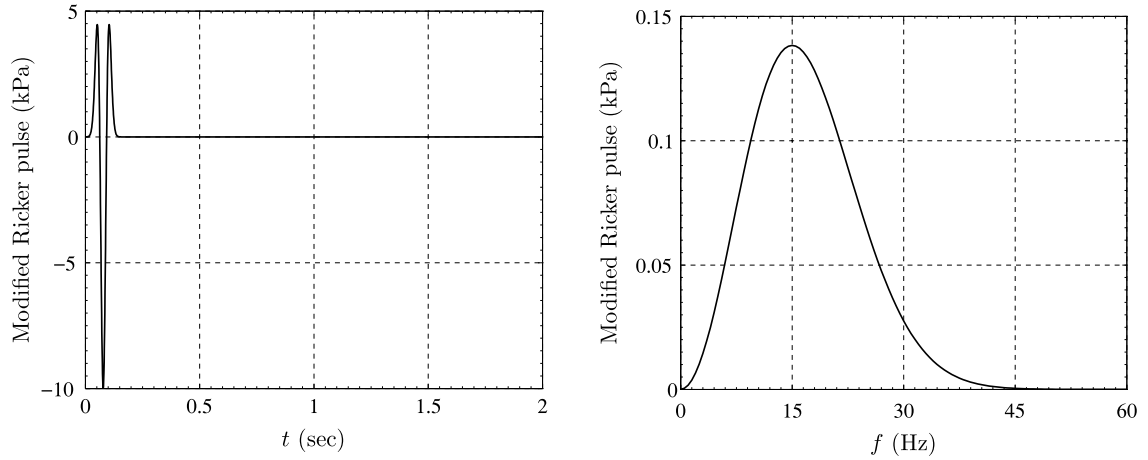
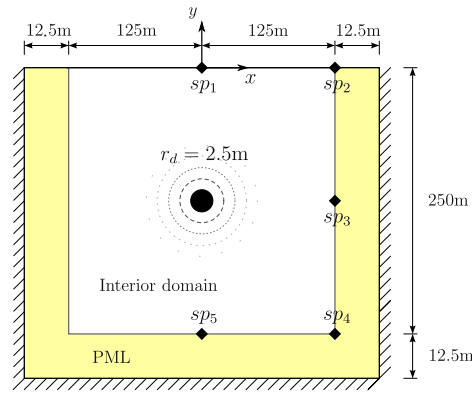**Fig. 4.** Ricker pulse time history and its Fourier spectrum.

Fig. 5. A PML-truncated semi-infinite homogeneous medium in two-dimensions subjected to an explosive *P*-wave source at the domain center.

corner blocks consist of the standard submatrices resulting from a displacement-only plane-strain formulation. This clearly suggests that to incorporate the effect of the PML into existing codes, one need only account for the submatrices in the lower parts of (34a) and (34b).

We remark that the symmetry of the mass-like, stiffness-like, and damping-like matrices in (34) has been preserved owing to the similar way the equations were complex-stretched. Retaining the symmetry of system matrices results in considerable computational savings. Moreover, our hybrid formulation requires less unknowns when compared to most mixed formulations (split- or unsplit-field) since the interior elastodynamics problem remains displacement-only.

As cast, the system matrices **M**, **C**, and **K** are symmetric and indefinite. However, a sign change in the lower blocks (corresponding to the stresses in the PML) can render the system matrices positive-definite, at the expense, however, of symmetry. For solution approaches employing iterative solvers, the positive-definiteness of the resulting system may offer an advantage. This alternative path is discussed next; to this end, we rewrite the semi-discrete form (33) as

$$\hat{\mathbf{M}}\ddot{\hat{\mathbf{d}}} + \hat{\mathbf{C}}\dot{\hat{\mathbf{d}}} + \hat{\mathbf{K}}\hat{\mathbf{d}} = \hat{\mathbf{F}}, \tag{35}$$

with the following definitions

$$\hat{\mathbf{M}} = \begin{bmatrix} \mathcal{M} & \mathbf{0} \\ \mathbf{0} & -\mathcal{N}_a \end{bmatrix}, \qquad \hat{\mathbf{C}} = \begin{bmatrix} \mathcal{C} & \mathcal{A} \\ -\mathcal{A}^T & -\mathcal{N}_b \end{bmatrix}, \qquad \hat{\mathbf{K}} = \begin{bmatrix} \mathcal{K} & \mathcal{B} \\ -\mathcal{B}^T & -\mathcal{N}_c \end{bmatrix}, \tag{36a}$$

$$\hat{\mathbf{d}} = \begin{bmatrix} \mathcal{U} & -\delta \end{bmatrix}^T, \qquad \hat{\mathbf{F}} = \mathbf{F}, \tag{36b}$$
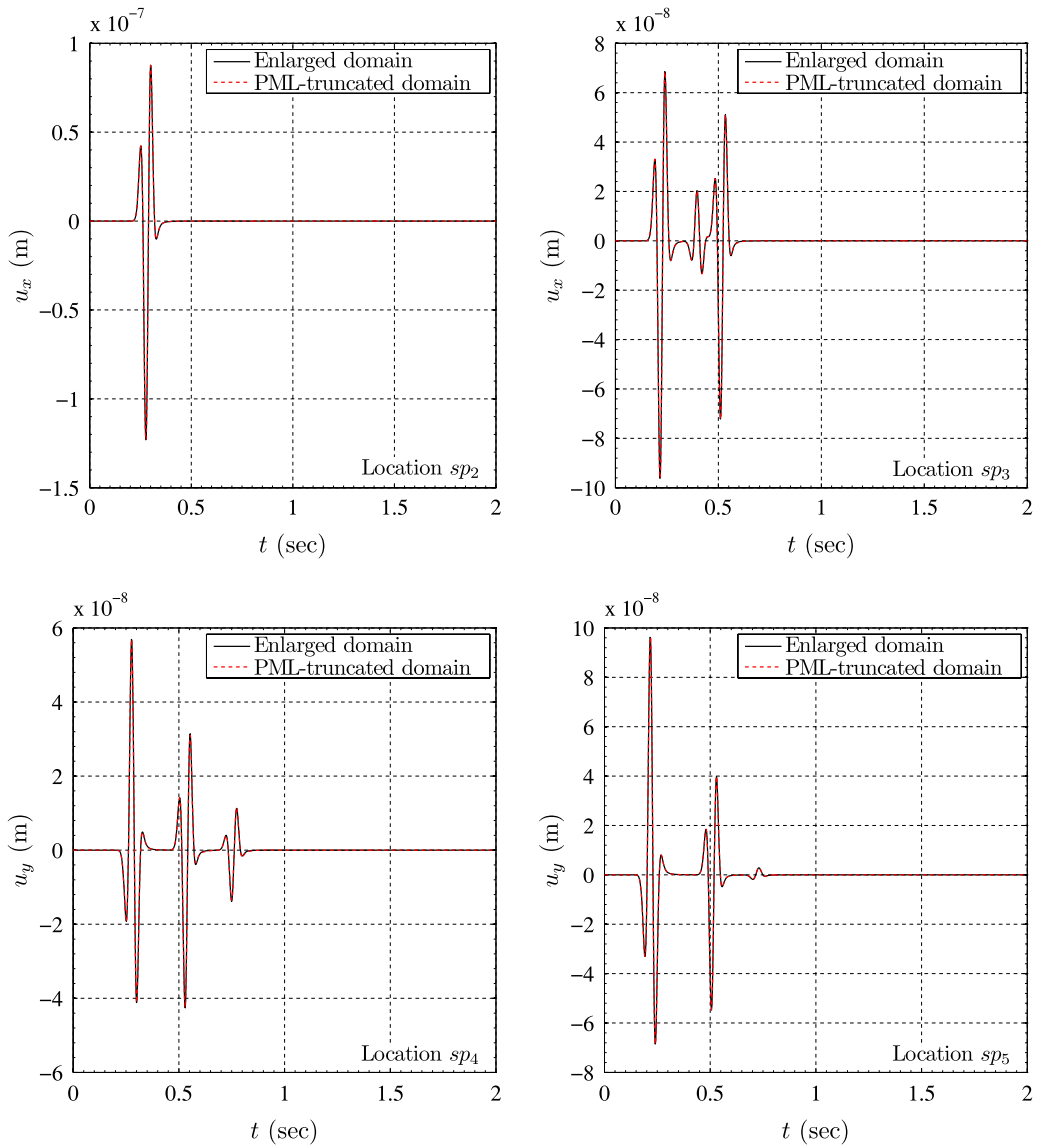
Fig. 6. Comparison of u_x and u_y time histories between the enlarged and PML-truncated domain solutions at various sampling points (homogeneous case).

where

$$\mathcal{M} = \begin{bmatrix} \mathbf{M}^{rr} & \mathbf{M}^{ri} & \mathbf{0} \\ & \mathbf{M}_a^{ii} & \mathbf{M}_a^{ip} \\ sym & & \mathbf{M}_a^{pp} \end{bmatrix}, \qquad \mathcal{C} = \begin{bmatrix} \mathbf{0} & \mathbf{0} & \mathbf{0} \\ & \mathbf{M}_b^{ii} & \mathbf{M}_b^{ip} \\ sym & & \mathbf{M}_b^{pp} \end{bmatrix},$$

$$\mathcal{K} = \begin{bmatrix} \mathbf{Q}^{rr} & \mathbf{Q}^{ri} & \mathbf{0} \\ & \mathbf{M}_c^{ii} & \mathbf{M}_c^{ip} \\ sym & & \mathbf{M}_c^{pp} \end{bmatrix}, \tag{37a}$$

$$\mathcal{N}_{(\cdot)} = \begin{bmatrix} \mathbf{N}_{(\cdot)}^{ii} & \mathbf{N}_{(\cdot)}^{ip} \\ (\mathbf{N}_{(\cdot)}^{ip})^T & \mathbf{N}_{(\cdot)}^{pp} \end{bmatrix}, \qquad \mathcal{A} = \begin{bmatrix} \mathbf{A}^{ii} & \mathbf{A}^{ip} \\ \mathbf{A}^{pi} & \mathbf{A}^{pp} \end{bmatrix}, \qquad \mathcal{B} = \begin{bmatrix} \mathbf{B}^{ii} & \mathbf{B}^{ip} \\ \mathbf{B}^{pi} & \mathbf{B}^{pp} \end{bmatrix}, \tag{37b}$$

$$\mathcal{U} = \begin{bmatrix} \mathbf{u}^r & \mathbf{u}^i & \mathbf{u}^p \end{bmatrix}^T, \qquad \mathcal{S} = \begin{bmatrix} \mathbf{S}^i & \mathbf{S}^p \end{bmatrix}^T. \tag{37c}$$

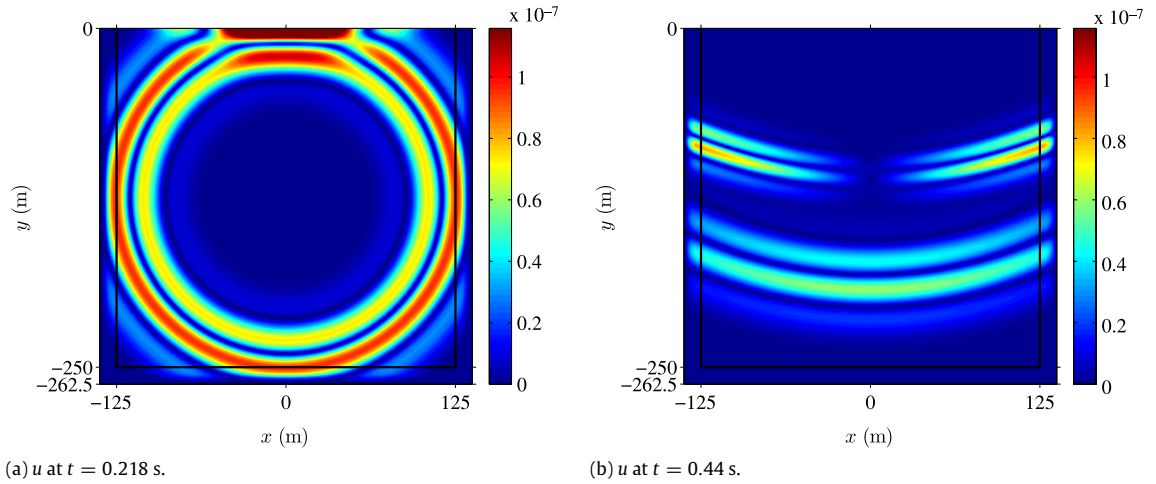(a) u at $t = 0.218$ s.　　　　　　　　　　　　　　　　　　(b) u at $t = 0.44$ s.

Fig. 7. Snapshots of u using an explosive Ricker pulse source at the center of the domain.

The new system matrices $\hat{\mathbf{M}}$, $\hat{\mathbf{C}}$, and $\hat{\mathbf{K}}$ are now unsymmetric. However, notice that their upper left diagonal submatrices $(\mathcal{M}, \mathcal{C}, \mathcal{K})$ are identical to the upper left diagonal submatrices of $\mathbf{M}$, $\mathbf{C}$, and $\mathbf{K}$: they are all positive-definite. Moreover, their off-diagonal block matrices ($\mathcal{A}$ and $\mathcal{B}$) have full rank, and, it can be, further, shown (see the Appendix) that the lower right diagonal submatrices ($-\mathcal{N}_a$, $-\mathcal{N}_b$, and $-\mathcal{N}_c$) are positive-definite. Therefore, the new matrices are unsymmetric and positive-definite (as shown, for example, in [34]). In other words, one can cast the problem in a manner that results in either symmetric and indefinite matrices, or in unsymmetric and positive-definite matrices. Both ways entail computational advantages, and the choice should be driven by the specifics of the application and the availability of resources (the choice of solvers also plays an important role). Here, for the applications, we prefer the symmetric formulation.

5. Numerical results

To test the accuracy and efficiency of the hybrid formulation, we discuss next two numerical experiments: a homogeneous semi-infinite domain, and a horizontally-layered medium with an elliptic inclusion. In both simulations, we apply a stress load, with a Ricker pulse time signature. The pulse is defined as

$$T_p(t) = \frac{(0.25u^2 - 0.5)e^{-0.25u^2} - 13e^{-13.5}}{0.5 + 13e^{-13.5}} \quad \text{with } 0 \le t \le \frac{6\sqrt{6}}{\omega_r}, \tag{38}$$

where

$$u = \omega_r t - 3\sqrt{6}, \tag{39}$$

and ω_r is the characteristic Ricker central circular frequency ($=2\pi f_r$) of the pulse. Here, we used $f_r = 15$ Hz, and an amplitude of 10 kPa as depicted in Fig. 4.

We provide three measures to quantify the PML's performance: (a) time history comparisons at select target locations; (b) decay of total energy inside the interior domain; and (c) time-dependent errors relative to a reference solution. To be able to compare the solutions of the PML-truncated domains, we create reference solutions by embedding the computational domain of interest Ω^{RD} within an *enlarged domain* Ω^{ED} with fixed exterior boundaries. The numerical solution within Ω^{ED} is obtained using a displacement-based formulation, in order to create a solution that is completely independent from the hybrid approach discussed herein. We retain the enlarged domain's solution up to times that are prior to the arrival of any waves to Ω^{RD} from the part of the domain that is exterior to Ω^{RD}. We then compare the reference and the hybrid method solutions only within the regular domain Ω^{RD} ($\subset \Omega^{\text{ED}}$).

To define the error metrics, we introduce first the time-dependent L^2 norm of the displacement field over an arbitrary domain Ω as

$$D(t; \Omega) = \left[\int_\Omega \mathbf{u}^T(\mathbf{x}, t)\mathbf{u}(\mathbf{x}, t)d\Omega\right]^{\frac{1}{2}}. \tag{40}$$

We define the time-dependent relative error metric $e(t)$ in terms of an L^2 norm, normalized with respect to the peak value of the aforementioned displacement field norm D, as

(a) Displacement norm $D(t; \Omega^{\mathrm{RD}})$.

(b) Relative error $e(t)$.

(c) Relative error for u_x at $sp2$.

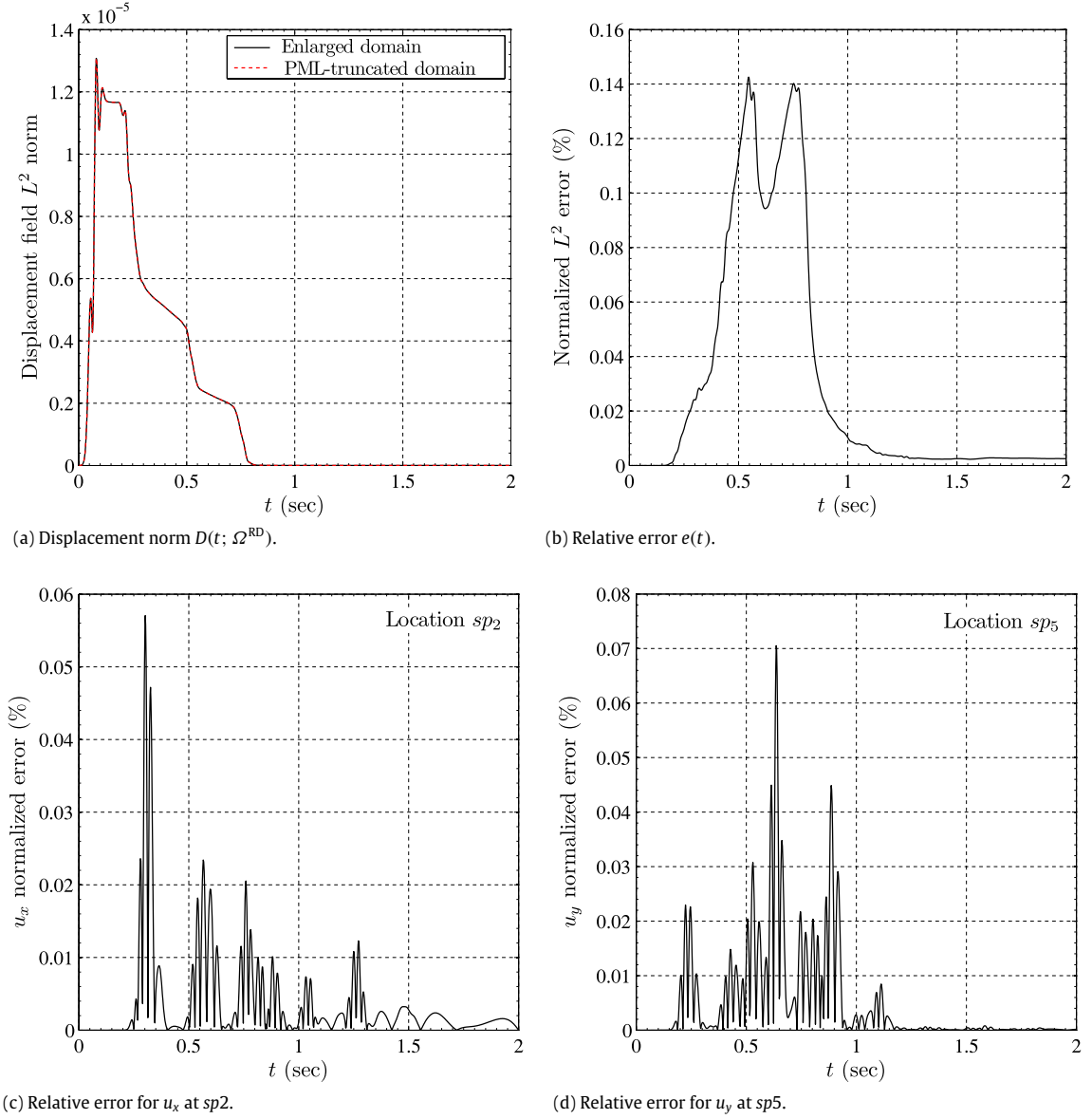(d) Relative error for u_y at $sp5$.

Fig. 8. Error metrics for the homogeneous domain case excited by an explosive Ricker pulse ($f_r = 15$ Hz) at the center of the domain.

$$e(t) = \frac{\left\{ \int_{\Omega^{\mathrm{RD}}} \left[\mathbf{u}(\mathbf{x}, t) - \mathbf{u}_{\mathrm{ED}}(\mathbf{x}, t) \right]^T \left[\mathbf{u}(\mathbf{x}, t) - \mathbf{u}_{\mathrm{ED}}(\mathbf{x}, t) \right] d\Omega \right\}^{\frac{1}{2}}}{\max_t D(t; \Omega^{\mathrm{RD}})} \times 100. \tag{41}$$

Lastly, we also study the decay of the total energy within the regular domain, along lines similar to the ones discussed by Komatitsch and Martin in [26]. In short, the energy, injected to the domain via the loading, is carried by waves that are absorbed and attenuated within the PML, and, thus, a rapid decay should be expected if the PML is working correctly. The total energy of the system as a function of time is expressed as

$$E_t(t) = \frac{1}{2} \int_\Omega \rho(\mathbf{x}, t) \left[\dot{\mathbf{u}}^T(\mathbf{x}, t) \dot{\mathbf{u}}(\mathbf{x}, t) \right] d\Omega + \frac{1}{2} \int_\Omega \left[\boldsymbol{\sigma}^T(\mathbf{x}, t) \boldsymbol{\epsilon}(\mathbf{x}, t) \right] d\Omega, \tag{42}$$

where $\dot{\mathbf{u}}, \boldsymbol{\sigma},$ and $\boldsymbol{\epsilon}$ are velocity, stress, and strain vectors, respectively. Similarly to $e(t)$, the total energy too is computed only within the regular domain Ω^{RD}.
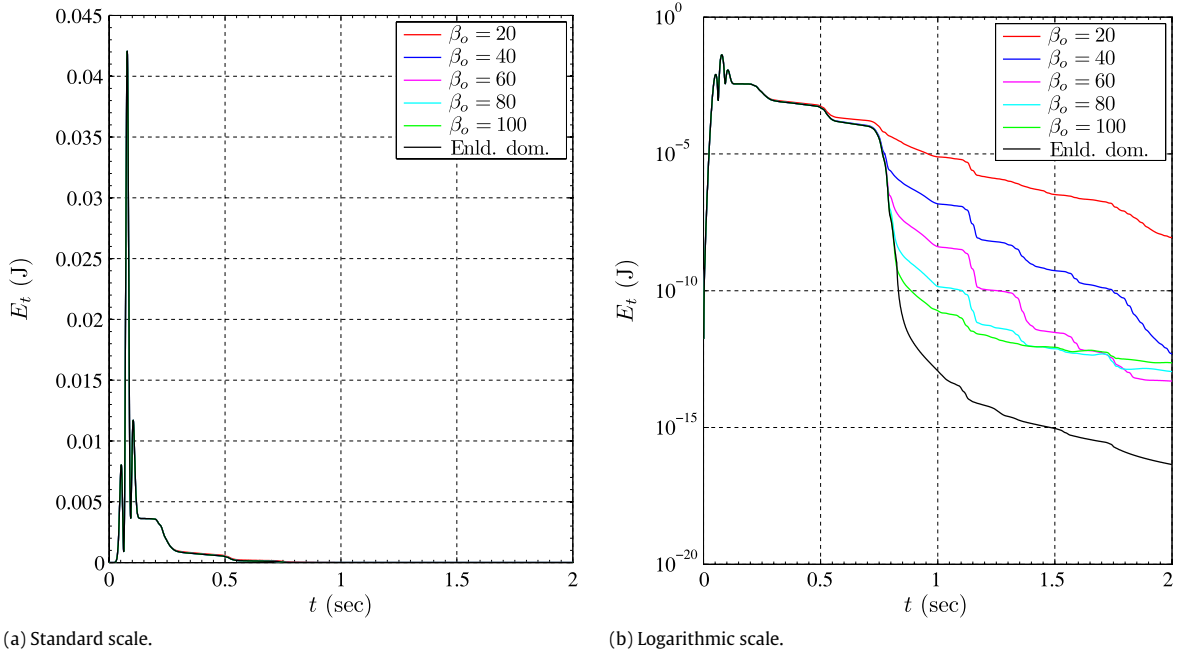
(a) Standard scale.

(b) Logarithmic scale.

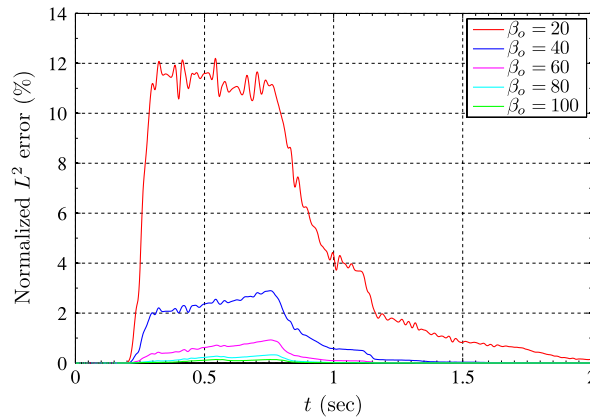**Fig. 9.** Total energy decay inside the regular domain (homogeneous case).

Fig. 10. Normalized time-dependent L^2 norm for various β_0 values.

5.1. Homogeneous media

We consider first a homogeneous half-plane with density $\rho = 2000$ kg/m^3, shear-wave velocity $c_s = 500$ m/s, and $\nu = 0.25$, that is reduced, through truncation, to a 250 m × 250 m computational domain, surrounded on its sides and bottom by a 12.5 m-thick PML, as shown in Fig. 5. We use an explosive P-wave source defined as

$$\mathbf{f}(\mathbf{x}, t) = \begin{cases} T_p(t) \left(1 - \dfrac{r^2}{r_d^2}\right)^3 \left(\dfrac{x - x_c}{r}, \dfrac{y - y_c}{r}\right), & (x, y) \in D_0, \\ 0, & (x, y) \notin D_0, \end{cases} \tag{43}$$

where T_p denotes the temporal part of the loading, $r = \sqrt{(x - x_c)^2 + (y - y_c)^2}$, and D_0 denotes the source disk of center (x_c, y_c) and radius r_d. For the temporal variation of the load we use the modified Ricker pulse depicted in Fig. 4. The explosive source disk's center was placed at 125 m below the surface, at the center of the domain. The PML and interior domains were discretized by quadratic quadrilateral elements with an element size of 1.25 m, whereas the disk was meshed with 0.625 m quadratic elements. The discretization resulted in a 10-cell-thick PML with a quadratic attenuation profile $m = 2$. The
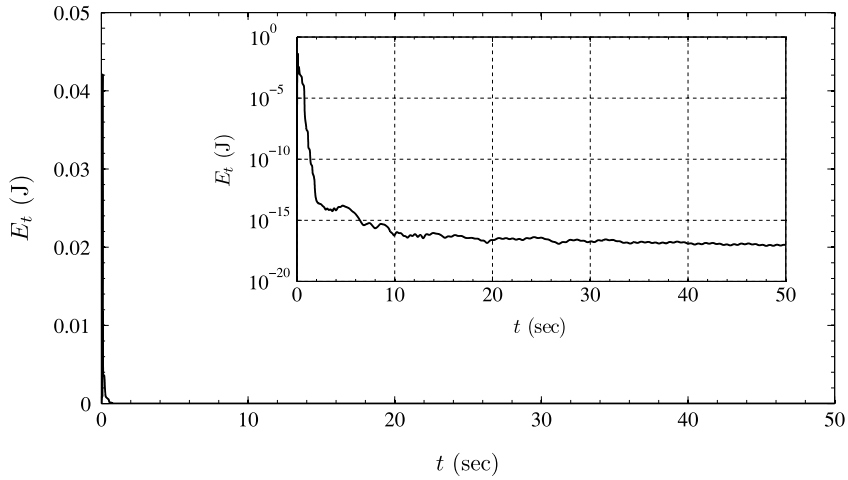
Fig. 11. Total energy decay inside the regular domain: standard scale; inset: logarithmic scale (homogeneous case).
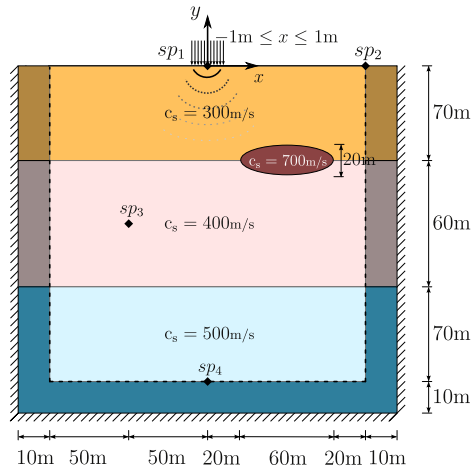

Fig. 12. A PML-truncated heterogeneous domain subjected to a surface load.

parameters β_o and α_o were set to 100 m/s and 0.75, respectively.[6] Using a time step of 0.001 s, we let the simulation run for 2 s and sample the time histories of the displacements at five locations sp_i, $i = 1 \cdots 5$.

To assess the validity of the hybrid PML-formulation, the displacement time histories at the sampling points were compared against the response obtained using the enlarged domain with fixed boundaries and a classic displacement-based plane-strain formulation. The enlarged domain's size was set to (1130 m × 565 m), and the observation time is limited so that reflections from its fixed exterior boundaries do not travel back and interfere with the wave motion solution in the computational domain of interest. Fig. 6 depicts the comparison of the response time histories for u_x and u_y at the various sp_i points. As can be seen, the agreement is excellent: the PML has effectively absorbed the waves without any reflections. It is also apparent from the figures that causality holds (sometimes an issue with PML implementations), and that the response is free of spurious reflections.

Fig. 7 shows snapshots of the displacements taken at two different times. In the figure on the left, the wave has impinged upon the free surface, and has also entered the side and bottom PML zones, which are shown in the figure with solid black lines that are indented with respect to the outer boundary. Notice that there are reflections from the free surface as expected (e.g. local doubling of the displacement amplitudes), and contrast them against the reflection-less side and bottom PML interfaces. The figure on the right corresponds to a later time and clearly shows two wave trains traveling towards the bottom: each wave train features three zones, with each zone corresponding to the amplitude peaks of the Ricker wavelet. Both wave trains (one P and one S) are reflections from the free surface. Again, notice that there are no discernible reflections

---

[6] Though an estimator for β_o has been provided in [14], α_o lacks such explicit form. Here, we favor a small stretch since evanescent waves are not dominant.
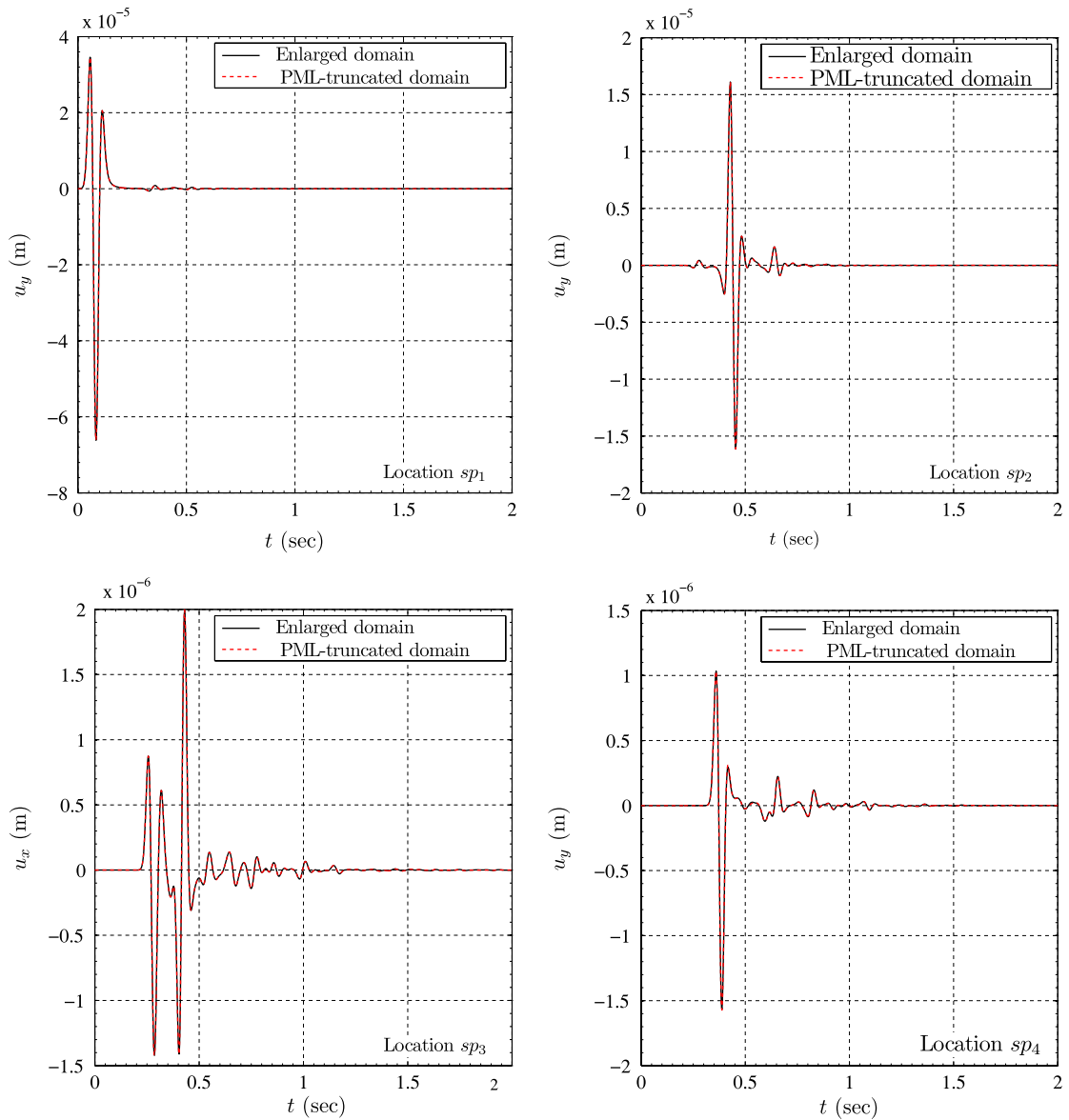
Fig. 13. Comparison of u_x and u_y time histories between the enlarged and PML-truncated domain solutions at various sampling points (heterogeneous case).

from the PML interfaces, nor any residual reflections from the fixed external boundaries that could have polluted the interior wave solution.

Fig. 8 depicts three different error metrics: Fig. 8(a) shows a visual comparison, displaying excellent agreement, between the reference solution and the PML-based solution for the displacement norm defined in (40); Fig. 8(b) shows the error norm defined in (41), which, at all times, is below 0.143%. Fig. 8(c) and (d) show the absolute value of the error at two distinct locations, normalized with respect to the absolute value of the peak record value; the error remains below 0.07% at all times.

Next, we study the effect the parameter β_o has on the quality of the obtained solutions. To this end, β_o was allowed to vary between 20 and 100, in multiples of 20, and the total energy decay (42) was computed for each one of the β_o values, as a function of time. Fig. 9 shows the energy decay plotted in standard (left), and semi-log scale (right), both terminated at 2 s. Shown on the same figure is the energy decay for all tested β_o values, as well as the reference decay corresponding to the enlarged domain (recall that this has been obtained using an independent displacement-based formulation).

Fig. 9 is quite revealing in several ways. First, almost all β_o values (except for $\beta_o = 20$) result in similarly sharp decay: after about 0.75 s, there is hardly any discernible residual energy left in the domain, since all the waves have traveled out
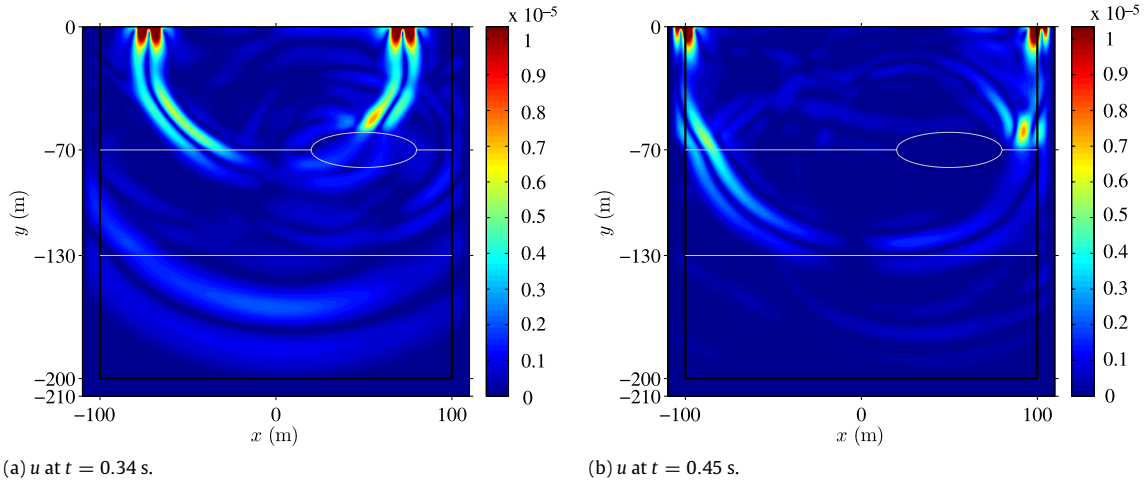
(a) u at $t = 0.34$ s.

(b) u at $t = 0.45$ s.

Fig. 14. Snapshots of u for the layered domain with an inclusion.

of the domain and have been absorbed by the PML. Second, a closer look, using the semi-log scale, reveals though that β_o plays a key role in determining the rate the energy decays, with lower β_o values enforcing slower decay. As β_o decreases, the fixed exterior PML boundaries reflect back waves of higher amplitude than those that would have resulted from higher β_o, first within the PML and later within the regular domain. Though still of small amplitude, when compared to the peak amplitudes observed in the regular domain, the reflections become amplified as they travel back into the regular domain (this is so by construction), and stand to pollute the solution and slow the energy decay. Thus, lower β_o values effectively decrease the absorptive capacity of the PML layer. Notice, lastly, that for $\beta_o = 100$ the remaining domain energy is lower than 10^{-12}, or roughly more than 10 orders of magnitude less than the peak domain energy, displaying effective wave absorption.

While the polynomial degree m controls the sharpness of the attenuation profile, the strength of decay inside the PML is determined by the parameter β_o. The energy plot seems to suggest that it is always beneficial to increase β_o to as large a value as possible. However, higher β_o values also introduce sharper PML decay profiles, as it can also be deduced from (4). That is, in sharper profiles, most of the wave absorption takes place within a small fraction of the PML length, right next to the PML-regular domain interface. For the absorption to be effective, it is critical that the mesh density within the PML adequately captures the sharp profile, to avoid the accumulation of numerical errors (the situation is similar to the difficulties arising when one attempts to approximate stress singularities with regular and inadequately sized isoparametric elements). In fact, sharper profiles are not only introduced by larger β_o, but arise also when lower polynomial degrees (m in (4)) are chosen. Though a detailed discussion and the necessary parametric study escapes the scope of this article, we remark that we have found linear profiles to be very sharp and should, in general, be avoided, in favor of, at least, quadratic, or preferably, quartic profiles. An optimal value of the β_0 parameter may very well exist. However, as can be seen from Fig. 10, where the normalized time-dependent L^2 norm (41) has been plotted for various β_0 values, the higher β_0 values result in very small errors. That is, for the range of values we considered, and provided that the mesh density within the PML can handle the sharper profiles imposed by the larger β_0 attenuation intensity factors, higher β_0 are preferable.

To illustrate the long-term stability of the proposed formulation, we let the simulation run for 50 s. As depicted in Fig. 11, no numerical instabilities were observed during the total simulation time of 50 s, i.e., for 50,000 time steps.

5.2. Heterogeneous media

To illustrate the performance of the PML in heterogeneous media, we consider a 200 m $\times$ 200 m layered medium with an elliptic inclusion as depicted in Fig. 12, which we truncate on its sides and bottom by 10 m-thick PML. A surface stress load with a Ricker pulse time signal ($f_r = 15$ Hz, amplitude of 10 kPa) is applied over a region (-1 m $\leq x \leq 1$ m). We define

$$
c_s(y) = \begin{cases} 300 \text{ m/s}, & \text{for } -70 \text{ m} \leq y \leq 0 \text{ m}, \\ 400 \text{ m/s}, & \text{for } -130 \text{ m} \leq y < -70 \text{ m}, \\ 500 \text{ m/s}, & \text{for } -210 \text{ m} \leq y < -130 \text{ m}, \\ 700 \text{ m/s}, & \text{for elliptic inclusion}, \end{cases} \tag{44}
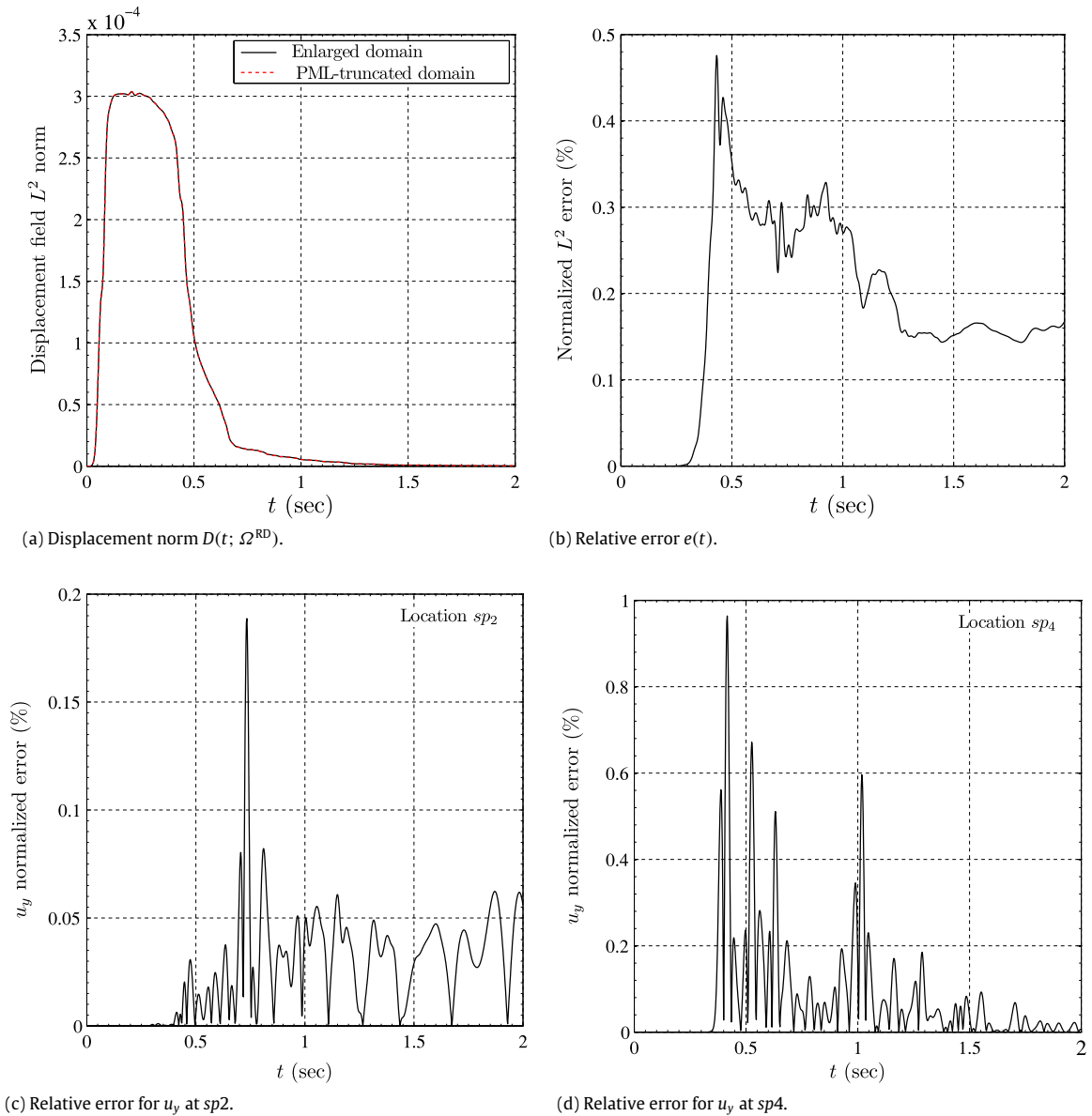$$

(a) Displacement norm $D(t; \Omega^{RD})$.

(b) Relative error $e(t)$.

(c) Relative error for u_y at $sp2$.

(d) Relative error for u_y at $sp4$.

Fig. 15. Error metrics for the layered medium excited by a surface Ricker pulse ($f_r = 15$ Hz) over a region (-1 m $\leq x \leq 1$ m).

with density $\rho = 2000$ kg/m^3 and $\nu = 0.25$. The material interfaces were extended horizontally into the PML, thereby, avoiding sudden material changes at the interface Γ^I. The PML and interior domains were discretized by quadratic quadrilateral elements with an element size of 1.0 m, whereas in the vicinity of the surface load, the interior domain was meshed with 0.25 m-elements. The parameter β_o was set to 80 m/s (as in the homogeneous case, we set $m = 2$ and $\alpha_o = 0.75$). Using a time step of 0.0005 s, we again simulated the wave motion for 2 s using the PML formulation, as well as a displacement-based formulation for an enlarged domain with fixed exterior boundaries.

To assess the performance of the hybrid PML formulation, we compare the displacement time histories at the sampling points against the reference solution obtained using the enlarged domain (900 m × 550 m). Fig. 13 depicts a visual comparison of the response time histories for u_x and u_y at various sp_i points. As can be seen, the agreement among the response time histories is quite satisfactory.

Fig. 14 shows the snapshots of the displacements taken at two different times ($t = 0.34$ and 0.45 s). We mark the layer and inclusion material interfaces with thin lines to ease visual examination. The layer boundaries are clearly visible due to reflections at the material interfaces. However, the critical interface Γ^I is free of reflections, and the hybrid PML formulation

(a) Standard scale.   (b) Logarithmic scale.
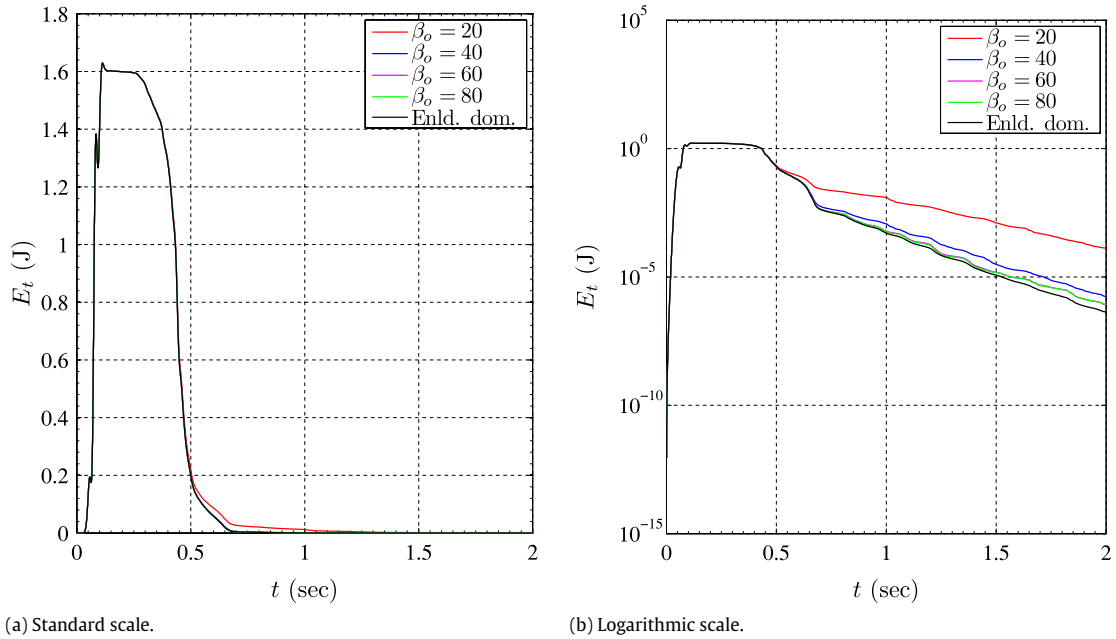
Fig. 16. Total energy decay inside the regular domain (heterogeneous case).

handles the interface waves properly. Extending the layer boundaries into the PML preserved the transparency of the PML-interior domain interface to the outgoing waves.

Next, we quantify the performance of the PML via the error metrics defined earlier. Fig. 15 is the counterpart of Fig. 8 for the heterogeneous case: the highest relative error in the L^2 norm is about 0.5%; though higher than the one we reported for the homogeneous case, we consider it satisfactory. The pointwise errors depicted in Fig. 15(c) and (d) are also quite pleasing: the error is less than about 1.0% at all times.

Lastly, Fig. 16 depicts the energy decay within the layered medium: in this case the decay is considerably more gradual than in the homogeneous case, since there are multiple reflections off of the layer interfaces that travel back to the free surface, reflect at the free surface, travel downwards to the first layer interface, partially reflect there, travel back to the free surface, and so on and so forth. We explored four different β_o values ($\beta_0 = 20, 40, 60$, and 80 m/s). The observed behavior is similar to the one discussed in the case of the homogeneous host: overall, the PML performance is excellent, with no discernible reflections or instabilities, even in the presence of heterogeneity.

6. Conclusions

We discussed a fully symmetric, hybrid formulation (mixed, coupled with a non-mixed approach) for the simulation of elastic waves in PML-truncated, arbitrarily heterogeneous media based on a regularly-stretched and unsplit-field PML. The resulting semi-discrete forms are second-order in time and symmetric, thus greatly facilitating time integration and leading to optimal computational cost (Table 2). An alternate form, which remains second-order in time, yet results in unsymmetric, but positive-definite matrices, is also possible by the same formulation. Existing displacement-based codes written for interior problems can be easily modified to accommodate PMLs as a means of domain truncation. We reported numerical simulations demonstrating the stability, efficacy, and cost-effectiveness of the hybrid formulation.

All simulations were conducted by adhering to the usual rules of thumb for wave simulations, whereby a minimum of 12 points per wavelength are necessary to adequately resolve the wave motion. The minimum expected wavelength was used to drive the mesh density. Having fixed the smallest element size, we then used the Courant condition to guide our choice of the time step.[7] However, we have found and reported that the sharpness of the decay profile within the PML may impose more onerous requirements on the PML's mesh density than those imposed from a wave propagation perspective. Detailed parametric studies are necessary for providing proper guidance on the choice of the PML parameters.

---

[7] The Courant condition is used to merely provide an indication for the time step; its satisfaction is not required, and time steps larger than those suggested by the Courant condition are possible.

Table 2
Computational cost comparison between fully-mixed (FM) and hybrid (H) formulations.

	Homogeneous	Heterogeneous	Generic
Elements	46,414	46,458	e
Nodes	140,101	140,247	n
r nodes	120,240	120,386	r
i nodes	1201	1201	i
p nodes	18,660	18,660	p
# of unknowns (FM)	700,505	701,235	$5r + 5(i + p)$
# of unknowns (H)	339,785	340,077	$2r + 5(i + p)$
Savings	51.5%	51.5%	$60\frac{r}{n}\%$

Acknowledgment

Appendix. Submatrices in Eq. (34)

The global system matrices are expressed in extended form as

$$
\mathbf{M} =
\begin{bmatrix}
\mathbf{M}^{rr} & \mathbf{0} & \mathbf{M}^{ri} & \mathbf{0} & \mathbf{0} & \mathbf{0} & \mathbf{0} & \mathbf{0} & \mathbf{0} & \mathbf{0} & \mathbf{0} & \mathbf{0} \\
 & \mathbf{M}^{rr} & \mathbf{0} & \mathbf{M}^{ri} & \mathbf{0} & \mathbf{0} & \mathbf{0} & \mathbf{0} & \mathbf{0} & \mathbf{0} & \mathbf{0} & \mathbf{0} \\
 & & \mathbf{M}^{ii} + \mathbf{M}_a^{ii} & \mathbf{0} & \mathbf{M}_a^{ip} & \mathbf{0} & \mathbf{0} & \mathbf{0} & \mathbf{0} & \mathbf{0} & \mathbf{0} & \mathbf{0} \\
 & & & \mathbf{M}^{ii} + \mathbf{M}_a^{ii} & \mathbf{0} & \mathbf{M}_a^{ip} & \mathbf{0} & \mathbf{0} & \mathbf{0} & \mathbf{0} & \mathbf{0} & \mathbf{0} \\
 & & & & \mathbf{M}_a^{pp} & \mathbf{0} & \mathbf{0} & \mathbf{0} & \mathbf{0} & \mathbf{0} & \mathbf{0} & \mathbf{0} \\
 & & & & & \mathbf{M}_a^{pp} & \mathbf{0} & \mathbf{0} & \mathbf{0} & \mathbf{0} & \mathbf{0} & \mathbf{0} \\
 & & & & & & -\mathbf{N}_{1a}^{ii} & \mathbf{N}_{2a}^{ii} & \mathbf{0} & -\mathbf{N}_{1a}^{ip} & \mathbf{N}_{2a}^{ip} & \mathbf{0} \\
 & & & & & & & -\mathbf{N}_{1a}^{ii} & \mathbf{0} & \mathbf{N}_{2a}^{ip} & -\mathbf{N}_{1a}^{ip} & \mathbf{0} \\
 & & & SYM & & & & & -\mathbf{N}_{3a}^{ii} & \mathbf{0} & \mathbf{0} & -\mathbf{N}_{3a}^{ip} \\
 & & & & & & & & & -\mathbf{N}_{1a}^{pp} & \mathbf{N}_{2a}^{pp} & \mathbf{0} \\
 & & & & & & & & & & -\mathbf{N}_{1a}^{pp} & \mathbf{0} \\
 & & & & & & & & & & & -\mathbf{N}_{3a}^{pp}
\end{bmatrix},
\tag{A.1a}
$$

$$
\mathbf{C} =
\begin{bmatrix}
\mathbf{0} & \mathbf{0} & \mathbf{0} & \mathbf{0} & \mathbf{0} & \mathbf{0} & \mathbf{0} & \mathbf{0} & \mathbf{0} & \mathbf{0} & \mathbf{0} & \mathbf{0} \\
 & \mathbf{0} & \mathbf{0} & \mathbf{0} & \mathbf{0} & \mathbf{0} & \mathbf{0} & \mathbf{0} & \mathbf{0} & \mathbf{0} & \mathbf{0} & \mathbf{0} \\
 & & \mathbf{M}_b^{ii} & \mathbf{0} & \mathbf{M}_b^{ip} & \mathbf{0} & \mathbf{A}_{\alpha yx}^{ii} & \mathbf{0} & \mathbf{A}_{\alpha xy}^{ii} & \mathbf{A}_{\alpha yx}^{ip} & \mathbf{0} & \mathbf{A}_{\alpha xy}^{ip} \\
 & & & \mathbf{M}_b^{ii} & \mathbf{0} & \mathbf{M}_b^{ip} & \mathbf{0} & \mathbf{A}_{\alpha xy}^{ii} & \mathbf{A}_{\alpha yx}^{ii} & \mathbf{0} & \mathbf{A}_{\alpha xy}^{ip} & \mathbf{A}_{\alpha yx}^{ip} \\
 & & & & \mathbf{M}_b^{pp} & \mathbf{0} & \mathbf{A}_{\alpha yx}^{pi} & \mathbf{0} & \mathbf{A}_{\alpha xy}^{pi} & \mathbf{A}_{\alpha yx}^{pp} & \mathbf{0} & \mathbf{A}_{\alpha xy}^{pp} \\
 & & & & & \mathbf{M}_b^{pp} & \mathbf{0} & \mathbf{A}_{\alpha xy}^{pi} & \mathbf{A}_{\alpha yx}^{pi} & \mathbf{0} & \mathbf{A}_{\alpha xy}^{pp} & \mathbf{A}_{\alpha yx}^{pp} \\
 & & & & & & -\mathbf{N}_{1b}^{ii} & \mathbf{N}_{2b}^{ii} & \mathbf{0} & -\mathbf{N}_{1b}^{ip} & \mathbf{N}_{2b}^{ip} & \mathbf{0} \\
 & & & & & & & -\mathbf{N}_{1b}^{ii} & \mathbf{0} & \mathbf{N}_{2b}^{ip} & -\mathbf{N}_{1b}^{ip} & \mathbf{0} \\
 & & & SYM & & & & & -\mathbf{N}_{3b}^{ii} & \mathbf{0} & \mathbf{0} & -\mathbf{N}_{3b}^{ip} \\
 & & & & & & & & & -\mathbf{N}_{1b}^{pp} & \mathbf{N}_{2b}^{pp} & \mathbf{0} \\
 & & & & & & & & & & -\mathbf{N}_{1b}^{pp} & \mathbf{0} \\
 & & & & & & & & & & & -\mathbf{N}_{3b}^{pp}
\end{bmatrix},
\tag{A.1b}
$$

$$\mathbf{K} = \begin{bmatrix}
\mathbf{Q}_1^{rr} & \mathbf{Q}_2^{rr} & \mathbf{Q}_1^{ri} & \mathbf{Q}_2^{ri} & \mathbf{0} & \mathbf{0} & \mathbf{0} & \mathbf{0} & \mathbf{0} & \mathbf{0} & \mathbf{0} & \mathbf{0} \\
& \mathbf{Q}_3^{rr} & (\mathbf{Q}_2^T)^{ri} & \mathbf{Q}_3^{ri} & \mathbf{0} & \mathbf{0} & \mathbf{0} & \mathbf{0} & \mathbf{0} & \mathbf{0} & \mathbf{0} & \mathbf{0} \\
& & \mathbf{Q}_1^{ii} + \mathbf{M}_c^{ii} & \mathbf{Q}_2^{ii} & \mathbf{M}_c^{ip} & \mathbf{0} & \mathbf{A}_{\beta yx}^{ii} & \mathbf{0} & \mathbf{A}_{\beta xy}^{ii} & \mathbf{A}_{\beta yx}^{ip} & \mathbf{0} & \mathbf{A}_{\beta xy}^{ip} \\
& & & \mathbf{Q}_3^{ii} + \mathbf{M}_c^{ii} & \mathbf{0} & \mathbf{M}_c^{ip} & \mathbf{0} & \mathbf{A}_{\beta xy}^{ii} & \mathbf{A}_{\beta yx}^{ii} & \mathbf{0} & \mathbf{A}_{\beta xy}^{ip} & \mathbf{A}_{\beta yx}^{ip} \\
& & & & \mathbf{M}_c^{pp} & \mathbf{0} & \mathbf{A}_{\beta yx}^{pi} & \mathbf{0} & \mathbf{A}_{\beta xy}^{pi} & \mathbf{A}_{\beta yx}^{pp} & \mathbf{0} & \mathbf{A}_{\beta xy}^{pp} \\
& & & & & \mathbf{M}_c^{pp} & \mathbf{0} & \mathbf{A}_{\beta xy}^{pi} & \mathbf{A}_{\beta yx}^{pi} & \mathbf{0} & \mathbf{A}_{\beta xy}^{pp} & \mathbf{A}_{\beta yx}^{pp} \\
& & & & & & -\mathbf{N}_{1c}^{ii} & \mathbf{N}_{2c}^{ii} & \mathbf{0} & -\mathbf{N}_{1c}^{ip} & \mathbf{N}_{2c}^{ip} & \mathbf{0} \\
& & & & & & & -\mathbf{N}_{1c}^{ii} & \mathbf{0} & \mathbf{N}_{2c}^{ip} & -\mathbf{N}_{1c}^{ip} & \mathbf{0} \\
& & & S\,Y\,M & & & & & -\mathbf{N}_{3c}^{ii} & \mathbf{0} & \mathbf{0} & -\mathbf{N}_{3c}^{ip} \\
& & & & & & & & & -\mathbf{N}_{1c}^{pp} & \mathbf{N}_{2c}^{pp} & \mathbf{0} \\
& & & & & & & & & & -\mathbf{N}_{1c}^{pp} & \mathbf{0} \\
& & & & & & & & & & & -\mathbf{N}_{3c}^{pp}
\end{bmatrix}, \tag{A.1c}$$

$$\mathbf{d} = \begin{bmatrix} \mathbf{u}_x^r & \mathbf{u}_y^r & \mathbf{u}_x^i & \mathbf{u}_y^i & \mathbf{u}_x^p & \mathbf{u}_y^p & \mathbf{S}_{xx}^i & \mathbf{S}_{yy}^i & \mathbf{S}_{xy}^i & \mathbf{S}_{xx}^p & \mathbf{S}_{yy}^p & \mathbf{S}_{xy}^p \end{bmatrix}^T, \tag{A.1d}$$

$$\mathbf{F} = \begin{bmatrix} (\mathbf{G}_x^r + \mathbf{Z}_x^r) & (\mathbf{G}_y^r + \mathbf{Z}_y^r) & (\mathbf{G}_x^i + \mathbf{Z}_x^i) & (\mathbf{G}_y^i + \mathbf{Z}_y^i) & \mathbf{0} & \mathbf{0} & \mathbf{0} & \mathbf{0} & \mathbf{0} & \mathbf{0} & \mathbf{0} & \mathbf{0} \end{bmatrix}^T. \tag{A.1e}$$

The various submatrices forming the above global system matrices are defined as follows:

$$\mathbf{M} = \int_{\Omega^{\mathrm{RD}}} \rho \boldsymbol{\Phi} \boldsymbol{\Phi}^T \, d\Omega, \tag{A.2a}$$

$$\mathbf{M}_k = \int_{\Omega^{\mathrm{PML}}} k \, \rho \boldsymbol{\Phi} \boldsymbol{\Phi}^T d\Omega, \quad k = a, b, c \tag{A.2b}$$

$$\mathbf{N}_{ik} = \begin{cases} \displaystyle\int_{\Omega^{\mathrm{PML}}} k \frac{\lambda + 2\mu}{4\mu(\lambda + \mu)} \boldsymbol{\Psi} \boldsymbol{\Psi}^T d\Omega, & i = 1, k = a, b, c, \\[2ex] \displaystyle\int_{\Omega^{\mathrm{PML}}} k \frac{\lambda}{4\mu(\lambda + \mu)} \boldsymbol{\Psi} \boldsymbol{\Psi}^T d\Omega, & i = 2, k = a, b, c, \\[2ex] \displaystyle\int_{\Omega^{\mathrm{PML}}} k \frac{1}{\mu} \boldsymbol{\Psi} \boldsymbol{\Psi}^T d\Omega, & i = 3, k = a, b, c, \end{cases} \tag{A.2c}$$

$$\mathbf{A}_{ijk} = \int_{\Omega^{\mathrm{PML}}} i_j \frac{\partial \boldsymbol{\Phi}}{\partial k} \boldsymbol{\Psi}^T d\Omega, \quad i = \alpha, \beta, j, k = x, y, \tag{A.2d}$$

$$\mathbf{Q}_i = \begin{cases} \displaystyle\int_{\Omega^{\mathrm{RD}}} \left[(\lambda + 2\mu) \frac{\partial \boldsymbol{\Phi}}{\partial x} \frac{\partial \boldsymbol{\Phi}^T}{\partial x} + \mu \frac{\partial \boldsymbol{\Phi}}{\partial y} \frac{\partial \boldsymbol{\Phi}^T}{\partial y} \right] d\Omega, & i = 1, \\[3ex] \displaystyle\int_{\Omega^{\mathrm{RD}}} \left[\lambda \frac{\partial \boldsymbol{\Phi}}{\partial x} \frac{\partial \boldsymbol{\Phi}^T}{\partial y} + \mu \frac{\partial \boldsymbol{\Phi}}{\partial y} \frac{\partial \boldsymbol{\Phi}^T}{\partial x} \right] d\Omega, & i = 2, \\[3ex] \displaystyle\int_{\Omega^{\mathrm{RD}}} \left[\mu \frac{\partial \boldsymbol{\Phi}}{\partial x} \frac{\partial \boldsymbol{\Phi}^T}{\partial x} + (\lambda + 2\mu) \frac{\partial \boldsymbol{\Phi}}{\partial y} \frac{\partial \boldsymbol{\Phi}^T}{\partial y} \right] d\Omega, & i = 3. \end{cases} \tag{A.2e}$$

Moreover, the global load vector submatrices are expressed as

$$\mathbf{G}_i = \int_{\Gamma_N^{\mathrm{RD}}} \boldsymbol{\Phi} \, g_i(\mathbf{x}, t) \, d\Gamma, \quad i = x, y, \tag{A.2f}$$

$$\mathbf{Z}_i = \int_{\Omega^{\mathrm{RD}}} \boldsymbol{\Phi} f_i(\mathbf{x}, t) \, d\Omega, \quad i = x, y. \tag{A.2g}$$

We remark that if in Eqs. (A.2) the integrations are carried out over a single element, then the equations represent element matrices. In particular, Eqs. (A.2b)–(A.2d), are the PML element matrices, if Ω^{PML} is replaced by a PML element. The superscripts in (A.1) are used to display the partitions of element submatrices. The ordering is done in such a way that the interior domain nodes come first, followed by the interface nodes, and the PML nodes come last. Thus, any element submatrix could be partitioned as

$$\Box_{el} = \begin{bmatrix} \Box^{rr} & \Box^{ri} \\ \Box^{ir} & \Box^{ii} \end{bmatrix} \quad \text{where } el \in \Omega^{\text{RD}}, \tag{A.3a}$$

$$\Box_{el} = \begin{bmatrix} \Box^{ii} & \Box^{ip} \\ \Box^{pi} & \Box^{pp} \end{bmatrix} \quad \text{where } el \in \Omega^{\text{PML}}. \tag{A.3b}$$

Similarly, the global load vector submatrices can be partitioned as

$$\Box_{el} = \begin{bmatrix} \Box^{r} \\ \Box^{i} \end{bmatrix} \quad \text{where } el \in \Omega^{\text{RD}}. \tag{A.3c}$$

Lastly, earlier in Section 4, we argued that each of $-\mathcal{N}_a$, $-\mathcal{N}_b$, and $-\mathcal{N}_c$ in (37) are positive-definite. To show this, it suffices to show that the following generic block is positive-definite:

$$\hat{\mathcal{N}}_{(\cdot)} = \begin{bmatrix} \mathbf{N}_{1.} & -\mathbf{N}_{2.} & \mathbf{0} \\ -\mathbf{N}_{2.} & \mathbf{N}_{1.} & \mathbf{0} \\ \mathbf{0} & \mathbf{0} & \mathbf{N}_{3.} \end{bmatrix}. \tag{A.4a}$$

Then, for any vector $\boldsymbol{q}^T = [\boldsymbol{q}_x \boldsymbol{q}_y \boldsymbol{q}_z]^T$, there results

$$\boldsymbol{q}^T \hat{\mathcal{N}}_{(\cdot)} \boldsymbol{q} = \boldsymbol{q}_x^T (\mathbf{N}_{1.} - \mathbf{N}_{2.}) \boldsymbol{q}_x + \boldsymbol{q}_y^T (\mathbf{N}_{1.} - \mathbf{N}_{2.}) \boldsymbol{q}_y + (\boldsymbol{q}_x^T - \boldsymbol{q}_y^T) \mathbf{N}_{2.} (\boldsymbol{q}_x - \boldsymbol{q}_y) + \boldsymbol{q}_z^T \mathbf{N}_{3.} \boldsymbol{q}_z. \tag{A.5}$$

The above quantity is positive, provided that $(\mathbf{N}_{1.} - \mathbf{N}_{2.})$ is positive-definite; from (A.2c) it follows that

$$\mathbf{N}_{1.} - \mathbf{N}_{2.} = \int_{\Omega^{\text{PML}}} (\cdot) \frac{1}{2(\lambda + \mu)} \boldsymbol{\Psi} \boldsymbol{\Psi}^T d\Omega, \tag{A.6}$$

which is positive-definite. This completes the proof.

References

[1] J.-P. Bérenger, A perfectly matched layer for the absorption of electromagnetic waves, J. Comput. Phys. 114 (1994) 185–200.
[2] W.C. Chew, W.H. Weedon, A 3D perfectly matched medium from modified Maxwell's equations with stretched coordinates, Microwave Opt. Technol. Lett. 7 (1994) 599–604.
[3] M. Kuzuoglu, R. Mittra, Frequency dependence of the constitutive parameters of causal perfectly matched anisotropic absorbers, IEEE Microw. Guided Wave Lett. 6 (12) (1996) 447–449.
[4] J.A. Roden, S.D. Gedney, An efficient FDTD implementation of the PML with CFS in general media, in: IEEE Antennas and Propagation Society International Symposium, vol. 3, 2000, pp. 1362–1365.
[5] F.L. Teixeira, W.C. Chew, Perfectly matched layer in cylindrical coordinates, in: Antennas and Propagation Society International Symposium Digest, vol. 3, IEEE, Montreal, Canada, 1997, pp. 1908–1911.
[6] W.C. Chew, J.M. Jin, E. Michielssen, Complex coordinate system as a generalized absorbing boundary condition, in: Proc. 13th Annu. Rev. Prog. Appl. Comp. Electromag., vol. 2, Monterey, CA, 1997, pp. 909–914.
[7] F.L. Teixeira, W.C. Chew, PML-FDTD in cylindrical and spherical grids, IEEE Microw. Guided Wave Lett. 7 (9) (1997) 285–287.
[8] F.L. Teixeira, W.C. Chew, Systematic derivation of anisotropic PML absorbing media in cylindrical and spherical coordinates, IEEE Microw. Guided Wave Lett. 7 (11) (1997) 371–373.
[9] L. Zhao, The generalized theory of perfectly matched layers (GT-PML) in curvilinear co-ordinates, Int. J. Numer. Modelling 13 (2000) 457–469.
[10] F.L. Teixeira, W.C. Chew, Complex space approach to perfectly matched layers: a review and some new developments, Int. J. Numer. Modelling 13 (2000) 441–455.
[11] W.C. Chew, Q.H. Liu, Perfectly matched layers for elastodynamics: a new absorbing boundary condition, J. Comput. Acoust. 4 (4) (1996) 341–359.
[12] F.D. Hastings, J.B. Schneider, S.L. Broschat, Application of the perfectly matched layer (PML) absorbing boundary condition to elastic wave propagation, J. Acoust. Soc. Am. 100 (5) (1996) 3061–3069.
[13] Q.H. Liu, Perfectly matched layers for elastic waves in cylindrical and spherical coordinates, J. Acoust. Soc. Am. 105 (4) (1999) 2075–2084.
[14] F. Collino, C. Tsogka, Application of the perfectly matched absorbing layer model to the linear elastodynamic problem in anisotropic heterogeneous media, Geophysics 66 (1) (2001) 294–307.
[15] E. Bécache, P. Joly, C. Tsogka, Fictitious domains, mixed finite elements and perfectly matched layers for 2D elastic wave propagation, J. Comput. Acoust. 9 (3) (2001) 1175–1202.
[16] D. Komatitsch, J. Tromp, A perfectly matched layer absorbing boundary condition for the second-order seismic wave equation, Geophys. J. Int. 154 (2003) 146–153.
[17] T. Wang, X. Tang, Finite-difference modeling of elastic wave propagation: a nonsplitting perfectly matched layer approach, Geophysics 68 (5) (2003) 1749–1755.
[18] U. Basu, A.K. Chopra, Perfectly matched layers for transient elastodynamics of unbounded domains, Int. J. Numer. Methods Eng. 59 (2004) 1039–1074.
[19] G. Cohen, S. Fauqueux, Mixed spectral finite elements for the linear elasticity system in unbounded domains, SIAM J. Sci. Comput. 26 (3) (2005) 864–884.
[20] G. Festa, J.-P. Vilotte, The Newmark scheme as velocity-stress time-staggering: an efficient PML implementation for spectral element simulations of elastodynamics, Geophys. J. Int. 161 (2005) 789–812.

[21] U. Basu, Explicit finite element perfectly matched layer for transient three-dimensional elastic waves, Int. J. Numer. Methods Eng. 77 (2009) 151–176.
[22] F.H. Drossaert, A. Giannopoulos, A nonsplit complex frequency-shifted PML based on recursive integration for FDTD modeling of elastic waves, Geophysics 72 (2) (2007) T9–T17.
[23] F.H. Drossaert, A. Giannopoulos, Complex frequency shifted convolution PML for FDTD modelling of elastic waves, Wave Motion 44 (7–8) (2007) 593–604.
[24] K.C. Meza-Fajardo, A.S. Papageorgiou, A nonconvolutional, split-field, perfectly matched layer for wave propagation in isotropic and anisotropic elastic media: stability analysis, Bull. Seismol. Soc. Am. 98 (4) (2008) 1811–1836.
[25] G. Festa, S. Nielsen, PML absorbing boundaries, Bull. Seismol. Soc. Am. 93 (2) (2003) 891–903.
[26] D. Komatitsch, R. Martin, An unsplit convolutional perfectly matched layer improved at grazing incidence for the seismic wave equation, Geophysics 72 (5) (2007) SM155–SM167.
[27] R. Martin, D. Komatitsch, S.D. Gedney, A variational formulation of a stabilized unsplit convolutional perfectly matched layer for the isotropic or anisotropic seismic wave equation, CMES 37 (3) (2008) 274–304.
[28] S. Kucukcoban, L. Kallivokas, Mixed perfectly-matched-layers for direct transient analysis in 2D elastic heterogeneous media, Comput. Methods Appl. Mech. Eng. 200 (1–4) (2011) 57–76.
[29] D. Correia, J.-M. Jin, On the development of a higher-order PML, IEEE Trans. Antennas Propag. 53 (12) (2005) 4157–4163.
[30] F. Collino, P.B. Monk, Optimizing the perfectly matched layer, Comput. Methods Appl. Mech. Eng. 164 (1998) 157–171.
[31] A. Bermúdez, L. Hervella-Nieto, A. Prieto, R. Rodríguez, An optimal perfectly matched layer with unbounded absorbing function for time-harmonic acoustic scattering problems, J. Comput. Phys. 223 (2007) 469–488.
[32] L.F. Kallivokas, J. Bielak, R.C. MacCamy, A simple impedance-infinite element for the finite element solution of the three-dimensional wave equation in unbounded domains, Comput. Methods Appl. Mech. Eng. 147 (1997) 235–262.
[33] F. Brezzi, A survey of mixed finite element method, in: D. Dwoyer, M. Hussaini, R. Voigt (Eds.), Finite Elements Theory and Application, Springer-Verlag, New York, 1988, pp. 34–49.
[34] M. Benzi, G.H. Golub, J. Liesen, Numerical solution of saddle point problems, Acta Numer. (2005) 1–137.